

1

Simulations of organic light emitting diodes

	1.1 Introduction.....	1-1
	1.2 Working principles of an OLED.....	1-2
	Electrodes • Charge transport layers • Blocking layers • Emission layer	
	1.3 Drift–diffusion equations.....	1-6
	Charges • Recombination • Excitons • Boundary conditions and numerical solution • Limitations	
	1.4 Master equation.....	1-9
	Single-carrier charge transport • Finite charge-carrier densities • Mobility and diffusion constant	
Pascal Kordt <i>Max Planck Institute for Polymer Research, Ackermannweg 10, Mainz 55128, Germany</i>	1.5 Kinetic Monte Carlo.....	1-10
	Variable step size method • Forbidden events • Efficiency and parallelization	
Peter Bobbert <i>Department of Applied Physics, Eindhoven University of Technology, P.O. Box 513, 5600MB, Eindhoven, The Netherlands</i>	1.6 Rates.....	1-12
	Charge transfer • Electron–hole recombination • Energy transfer	
Reinder Coehoorn <i>Department of Applied Physics, Eindhoven University of Technology, P.O. Box 513, 5600MB, Eindhoven, The Netherlands</i>	1.7 Density of states.....	1-14
	Gaussian disorder • Perturbative approach • Hybrid approaches	
Falk May <i>BASF SE, GME/MC - B009, 67056 Ludwigshafen, Germany</i>	1.8 Reorganization energy.....	1-16
	1.9 Electronic coupling elements.....	1-17
	1.10 Morphology.....	1-17
	Classical force fields • Morphology simulations	
Christian Lennartz <i>TrinamiX GmbH, J542N, 67056 Ludwigshafen, Germany</i>	1.11 Scale bridging.....	1-19
	Stochastic models • Parametrization of Gaussian disorder models • Tabulated mobilities	
Denis Andrienko <i>Max Planck Institute for Polymer Research, Ackermannweg 10, Mainz 55128, Germany</i>	1.12 Case studies.....	1-24
	Current–voltage characteristics • Impedance spectroscopy • Efficiency • Electroluminescence of a white OLED • Degradation	
	1.13 Outlook.....	1-41
	Acknowledgments.....	1-42
	References.....	1-42

1.1 Introduction

The Nobel Prize in Physics 2014 was awarded “for the invention of efficient blue light-emitting diodes (LEDs) which has enabled bright and energy-saving white light sources” [Aka15, Ama15, Nak15], setting a clear target to mankind: energy-efficient and environmental-friendly light sources [For04]. The first *organic* light emitting diode was reported in 1987 by a team at

Kodak [TV87]. This publication, cited by now more than ten thousand times, stipulated the entire field of organic electronics. Shortly afterwards, a polymer LED (PLED) has been demonstrated [FBB90], paving the way for flexible lighting applications [CEV13]. Nowadays, OLEDs are successfully used in displays of mobile phones and televisions: In 2008 Samsung announced a flexible display that was only 50 μm thick [Ota08], about half the thickness of a sheet of paper. A prototype of an OLED display for the automotive market has been presented recently by Continental [Mer14]: in OLED displays black pixels are completely switched off, allowing the driver's eye to adapt better to the darkness. Contrary to liquid crystal displays (LCDs), OLED screens do not require backlight illumination, yielding exceptionally good contrast ratios and reduced power consumption. OLED displays also provide viewing angles and response times superior to LCDs and are, in general, thinner and lighter. Last but not least, many organic materials can be printed from solution, enabling cost-effective large-scale manufacturing on mechanically flexible films.

The prime challenge in OLED development is an improvement of device operation lifetimes. In many cases the steady decrease of luminescence efficiency of OLEDs under continuous operation is compensated by a gradual rise in bias voltages, or by using larger pixel sizes which can then be operated at lower voltages and luminances. Especially blue phosphorescent devices, with their high energy of emitted photons and long-lived excited states, are prone to fast material degradation. The underlying mechanisms of degradation, discussed in Section 1.12.5, are unfortunately not fully understood.

Designing new organic materials is crucial for tuning OLED properties, performance, and stability. One therefore needs to provide rigorous links between device characteristics and the chemical composition of the layers, or structure–property relationships. This can be done with the help of cheminformatics tools [OAABH⁺11], i.e., by correlating available experimental data to underlying chemical structures. However, the number of experimental samples is normally limited to a few hundred since synthesis, device optimization, and characterization are often costly and time consuming. A substantial extension of the training set is therefore experimentally not feasible to achieve, again motivating the development of computer simulations techniques capable of predicting device characteristics *in silico* [DSL15]. In this chapter we aim to provide an overview of theoretical models and simulation approaches developed to study charge and exciton transport in organic semiconductors, as well as to predict and eventually optimize current–voltage characteristics, electroluminescence efficiency, and lifetimes of OLEDs.

1.2 Working principles of an OLED

We will start by reviewing the elementary processes taking place in an OLED. The simplest two-layer OLED consists of hole and (luminescent) electron transporting layers, which are sandwiched between two electrodes, as shown in Figure 1.1(a). When a voltage is applied to the electrodes, holes are injected from the anode into the hole transporting layer (HTL) and electrons from the cathode into the electron transporting layer (ETL). The external field forces electrons and holes to drift towards the interface between these layers, where they recombine and emit light. Energetically, such a heterojunction is designed to facilitate the hole injection from HTL to ETL as well as to block electron diffusion into the opposite direction.

To fine-tune device properties such as luminescence, driving voltage, light outcoupling, and lifetime, more layers are added to a two-layer OLED: A typical phosphorescent OLED is shown in Figure 1.1(b). Here, when a voltage is applied to the electrodes, electrons are injected from the reflective metal cathode (Al) and holes from the semi-transparent anode (ITO). The cathode has a low work function while the anode has a high one. This energy difference is compensated by the externally applied voltage which forces charge carriers to drift into the emission layer. In the emission layer, holes and electrons form excitons, predominantly on the emitter (guest) molecules. Finally, radiative decay of an exciton leads to light emission. In the next sections we

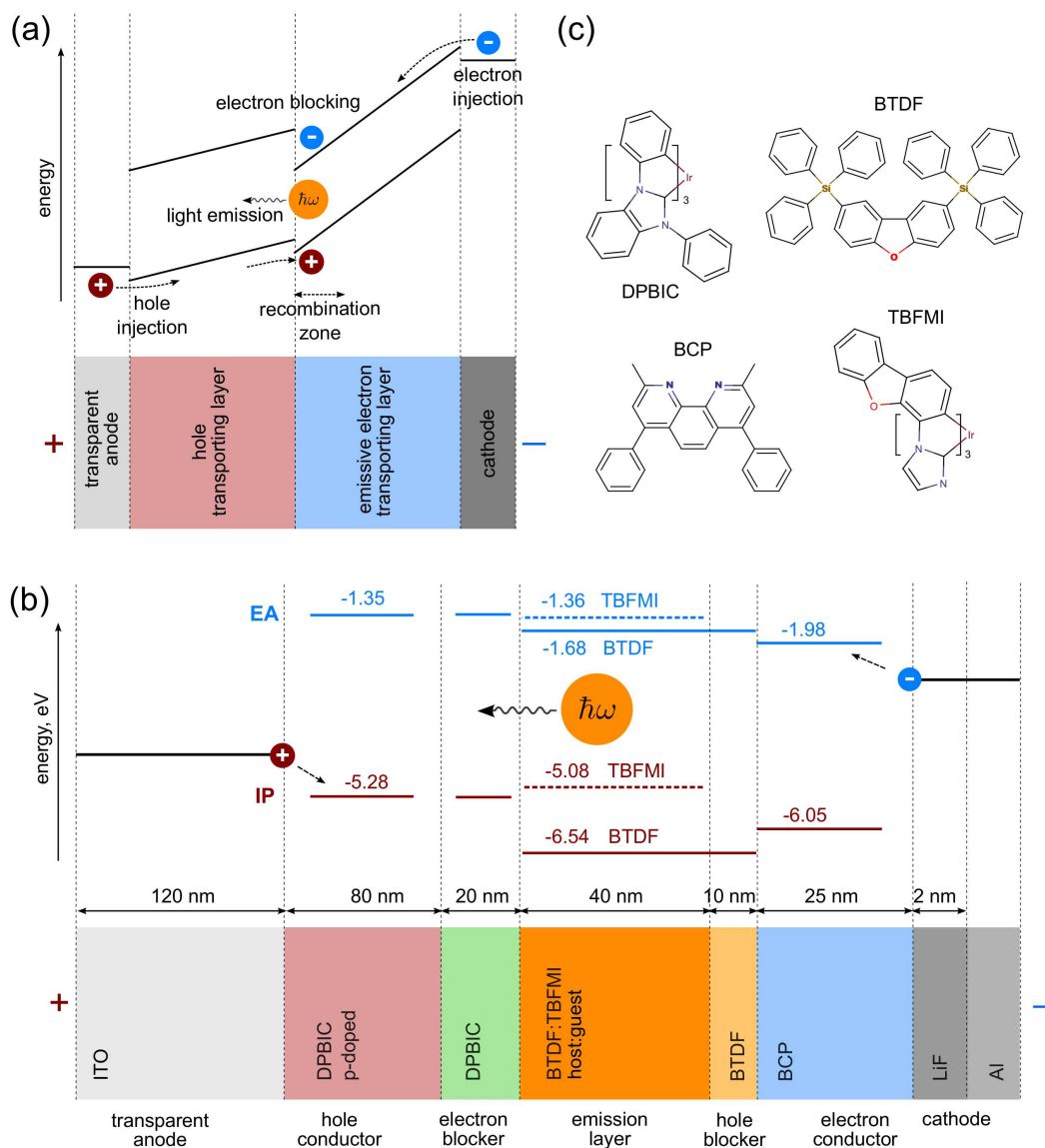


FIGURE 1.1 (a) Schematic of a two-layer electroluminescent OLED and its energy level diagram under applied voltage. (b) Structure of a blue phosphorescent OLED with a transparent anode (ITO), a reflective cathode (Al), emission layer, and hole/electron conduction/blocking layers. Indicated energy levels are without the applied bias. (c) Compounds used in the OLED (b). Adapted with permission from *Adv. Funct. Mater.*, 2015, 25, pp 1955–1971 (adapted version).

briefly review the functionality of all layers.

1.2.1 Electrodes

The outermost layers, metallic or metal-oxide electrodes, inject electrons and holes into organic layers. A common material for the semi-transparent anode is indium tin oxide (ITO) [Yer04]. Its low ionization potential ensures efficient hole injection into the organic layer. For efficient electron injection a low work function cathode is required. Since such materials are often air-unstable, normally bilayered structures are used [DXQ11], e.g. Al/LiF [FDK02, ZQP⁺02] or Ag/MgAg [ABF⁺01, KYF02].

1.2.2 Charge transport layers

The role of electron and hole transport layers is to provide an Ohmic contact to the electrodes (barrierless injection) and to help controlling light outcoupling. These layers are often doped: By inserting electron donating or accepting impurities into a material, their intrinsic charge carrier density is increased, leading to higher conductivities and a reduction of the injection barrier. While it is a standard technique in inorganic semiconductors, it can be challenging in organic materials: dopant molecules create energetic traps, hindering the formation of mobile charges [GCC04].

Realizing *p*-type doping, which increases the hole density, requires a dopant material with a lowest unoccupied molecular orbital (LUMO) level close to the highest occupied molecular orbital (HOMO) of the host. This is feasible in most cases and, consequently, it is used in many OLEDs. For example, the OLED stack in Figure 1.1(b) has a *p*-doped DPBIC hole transport layer. On the contrary, *n*-type doping requires a dopant material with a HOMO level near or above the LUMO of the host. The necessity to find air-stable dopant materials with such a high HOMO level makes *n*-type doping challenging. Moreover, when using small molecules such as O₂, Br₂, I₂ as dopant materials, these can diffuse into an organic host, leading to undesired doping profiles. This effect, however, can also be used to actually dope the adjacent layer with an interlayer of dopant molecules. In the stack shown in Figure 1.1(b) this technique is applied: Here a LiF interlayer is placed between the aluminium cathode and the electron transport layer, doping the latter [WMPL07]. Alq₃ (aluminum-tris(8-hydroxyquinolin)) is a material that can be used for both the hole- and the electron conducting layers. In the stack in Figure 1.1b DPBIC is used for hole conduction and BCP (bath-ocuproine-4,7-diphenyl-2,9-dimethyl-1,10-phenanthroline) serves as an electron-conducting layer [ABF⁺01, BLB⁺99, KYF02, NHBB⁺03, FDK02].

1.2.3 Blocking layers

Hole/electron blocking layers suppress charge flow to the opposite electrodes, enhancing their recombination probability in the emission layer. The hole blocking layer has an ionization potential (IP) lower than the IP of the emission layer. Similarly, an electron blocking layer has an electron affinity (EA) higher than the EA of the emission layer. In Figure 1.1 DPBIC is used as an electron blocker and BCP as a hole blocker [ABF⁺01, BLB⁺99, KYF02, NHBB⁺03, FDK02].

1.2.4 Emission layer

In the emission layer electrons and holes recombine, leading to exciton formation. Upon radiative decay of the excitons, photons are emitted. To avoid exciton quenching emitter (host molecules) are embedded into a matrix (guest molecules): In the stack shown in Figure 1.1(b), TBFMI is a blue phosphorescent emitter, while BTDF is the host material.

Exciton generation and the emission of photons proceeds in several steps, which are illustrated

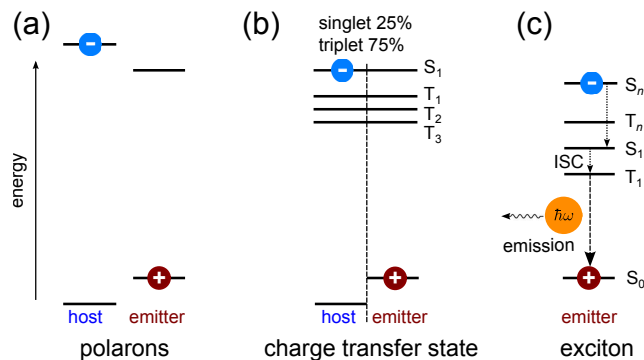


FIGURE 1.2 Exciton formation in the emission layer of a phosphorescent OLED. (a) Electron moves towards a hole which is trapped on the emitter molecule. (b) Charge transfer state is formed with the electron on a host and hole on a neighboring emitter molecule. Spins of hole and electron are already correlated to one singlet and three triplet states. (c) exciton is formed on the emitter molecule with a statistical probability to be in a 25% singlet and 75% triplet state. Singlet state undergoes fast intersystem crossing (ISC) into a triplet state which then emits light.

in Figure 1.2. First, a carrier (in this case a hole) is trapped on an emitter molecule and an oxidized complex is formed. Driven by Coulomb forces, a carrier of opposite charge (electron) moves on host molecules towards the trapped carrier. When the electron reaches a host molecules neighboring the oxidized emitter, a charge transfer (CT) state is formed, as shown in Figure 1.2 (b). In a CT state, the short-range exchange interaction leads to an energy splitting of singlet (S) and triplet (T) states. The triplet consists of three triplet substates, which differ from each other by their relative spin orientations. Statistically, one obtains a population ratio of 1:3 between singlet and triplet substates. In a final step, the electron moves in a very fast process directly to the emitter molecule, forming an excited emitter (Figure 1.2 (c)). This process may occur via a singlet or a triplet path, depending on the initial spin orientation of the electron–hole pair. The two spins of an electron and a hole are then coupled to four new combined states: One singlet state, with total spin momentum 0, and one triplet state, with the total spin momentum 1. In a statistical limit, all four substates are populated with an equal probability.

An exciton formed on an emitter molecule can decay radiatively by fluorescence or phosphorescence. In *fluorescence*, which is the most common radiative decay pathway for organic molecules, the radiative decay occurs from the excited singlet state, S_1 , to the ground state. If triplet states are not harvested, the internal quantum efficiency of an OLED is limited to 25%. *Phosphorescence*, conversely, allows to harvest triplet states. One can use compounds with large spin–orbit couplings, such as organometallic complexes, to achieve this: The large spin–orbit coupling capacitates a spin flip (see Figure 1.2(c)), leading to *intersystem crossing* (ISC), i.e., a transition between singlet and triplet states. Thus, also triplets can decay radiatively ($T_1 \rightarrow S_0$), yielding an internal quantum efficiency of 100%.

Another way of harvesting triplet states is via a *thermally-activated delayed fluorescence* (TADF) [PLZ⁺13]. TADF can be realized in organic molecules even with small spin–orbit coupling. In TADF triplets are converted to singlets thermally (reverse intersystem crossing) and a radiative $S_1 \rightarrow S_0$ decay (fluorescence) takes place. TADF requires small energy differences between T_1 and S_1 levels $\Delta E_{ST} \sim k_B T$. To achieve this, a large spatial HOMO-LUMO separation is required. This, however, competes with the requirement of large oscillator strengths of fluorescence, i.e., large a transition dipole moment [HSM⁺15].

Several processes in an OLED can lead to efficiency losses. In a phosphorescent OLED these are *triplet–triplet quenching*, where two triplets annihilate as a result of the interaction of neigh-

boring excited emitter molecules, and *triplet-polaron quenching*, i.e., an interaction between electronic and vibrational modes, energy transfer to polarons and dissociation into free carriers [RWL07, Yer04]. These processes are discussed in more detail in Sections 1.12.3 and 1.12.5.

A comprehensive OLED model should incorporate all the aforementioned elementary processes: charge injection from electrodes, charge trapping and transport to the emission layer, long-range electron-hole interactions, formation of a charge transfer and excited states, exciton-exciton and exciton-polaron interactions, and radiative decay of excitons. The ultimate goal of such a model is to predict the current-voltage-luminescence characteristics of the multilayered OLED structure. Since the typical thickness of an organic layer of an OLED stack ranges from 10 to 100 nm, it is computationally prohibitive to use only first principles methods for OLED modeling. State of the art OLED simulations employ either continuous models, such as drift-diffusion equations (see Section 1.3), or solve the master equation for charge/exciton occupation probabilities (see Section 1.4). Both approaches use models of different complexity. For example, if the target is to optimize the composition of the stack made of well-characterized organic layers, drift-diffusion equations and lattice models with phenomenologically-fitted parameters are used. If one also needs to retain the link to the underlying chemical composition of layers, off-lattice models based on first principles parametrizations are required. In all cases we are dealing with a typical multiscale problem, which requires the development of scale-bridging techniques (see Section 1.11). In the next sections we review these approaches, paying special attention to limitations, parametrizations, and scale-bridging issues.

1.3 Drift-diffusion equations

We will start with the most coarse model: on a macroscopic level, the drift and diffusion of electrons, holes, and excitons in an OLED stack can be described by the corresponding densities, denoted here as n , p , and s , respectively. The drift-diffusion model assumes that local charge densities, charge mobilities, μ_n , μ_p , diffusion constants, D_e , D_n , and field strength, F , all vary continuously in space. The set of equations describing the time-dependent spatial distribution of charge and exciton densities is then based on the respective conservation laws. In what follows we describe a model where charges drift-diffuse in a given density of states $g(E)$ (see also sec. 1.7), can be trapped, have density- and field-dependent mobilities, and recombine either radiatively or non-radiatively.

1.3.1 Charges

Charge conservation leads to two continuity equations, for electrons and holes

$$e \frac{\partial n}{\partial t} = \vec{\nabla} \cdot \vec{J}_n - eR(n, p) - e \frac{\partial n_t}{\partial t}, \quad e \frac{\partial p}{\partial t} = -\vec{\nabla} \cdot \vec{J}_p - eR(n, p) - e \frac{\partial p_t}{\partial t}, \quad (1.1)$$

where $R(n, p)$ is the recombination rate (see Section 1.3.2), n_t and p_t are densities of trapped charges and e is the electron charge. The current equations for electron and holes drift-diffusion in an electrostatic potential ψ read [KHSR10, RKP⁺11]

$$\vec{J}_n = -en\mu_n \vec{\nabla} \psi + eD_n \vec{\nabla} n, \quad \vec{J}_p = -ep\mu_p \vec{\nabla} \psi - eD_p \vec{\nabla} p. \quad (1.2)$$

Note that only mobile charges contribute to the current. Summing up electron and hole currents yields the total current in the device, $\vec{J} = \vec{J}_n + \vec{J}_p$. The electrostatic potential ψ is related to the electron and hole densities via the Poisson equation

$$\varepsilon_0 \varepsilon_r \Delta \psi = e(n - p + n_t - p_t), \quad (1.3)$$

where ε_0 is the vacuum and ε_r is the relative permittivity. The densities of trapped charges obey the phenomenological rate equations

$$\frac{\partial n_t}{\partial t} = r_{c,n}n(N_t - n_t) - r_{e,n}n_t, \quad \frac{\partial p_t}{\partial t} = r_{c,p}p(N_t - p_t) - r_{e,p}p_t, \quad (1.4)$$

where it is assumed that traps occupy two levels (one for holes and one for electrons). Here N_t is the trap density, r_e is the escape rate and r_c the capture rates of electrons (n) and holes (p), respectively.

Since two electrons or holes cannot occupy the same energy level at the same time, the occupation probabilities of energy levels follow the Fermi–Dirac statistics [KQ93]

$$f(E, E_F) = \left[1 + \exp\left(\frac{E - E_F}{k_B T}\right) \right]^{-1}, \quad (1.5)$$

where $f(E, E_F)$ is the occupation probability of a level with energy E , k_B is the Boltzmann constant and T the temperature. The carrier density is then related to the quasi-Fermi level, E_F , as

$$p(E_F) = \frac{N}{V} \int_{-\infty}^{\infty} g(E)f(E, E_F)dE, \quad (1.6)$$

where $g(E)$ is the density of states (see Section 1.7), N is the number of holes, and V the box volume. Similar relation holds also for electrons. Fermi–Dirac statistics implies that the diffusion coefficient and mobility in Equation (1.1) are related via the generalized Einstein relation [RT02]

$$D = \frac{p\mu}{e} \left(\frac{\partial p}{\partial E_f} \right)^{-1}. \quad (1.7)$$

In order to solve the drift–diffusion equations one needs to know the dependence of mobility on charge density, electric field, and temperature, $\mu(p, n, \vec{F}, T)$. These can be obtained either from experiments or Monte Carlo simulations, as discussed in Section 1.11.

1.3.2 Recombination

The recombination rate $R(n, p)$ includes two loss mechanisms: Shockley–Read–Hall (SRH), or trap-assisted recombination, and bimolecular recombination. In SRH recombination, electrons are trapped in low energy states and recombine with free holes. The macroscopic rate for this process reads [LRF14]

$$R_{\text{SRH}} = \frac{C_n C_p N_t (np - n_i p_i)}{C_n (n + n_i) + C_p (p + p_i)}. \quad (1.8)$$

Here C_n and C_p are the capture coefficients for electrons and holes, respectively, N_t is the trap density for electrons, n and p the electron and hole densities, and n_i and p_i are the intrinsic electron and hole densities.

Bimolecular recombination is often modeled using the Langevin rate

$$R_L = \gamma(np - n_i p_i), \quad \gamma = \frac{q}{\varepsilon_0 \varepsilon_r} (\mu_n + \mu_p) \quad (1.9)$$

Here γ is the recombination constant and μ_n and μ_p are electron and hole mobilities. The intrinsic electron and hole carrier densities are often neglected [PRR⁺12, LRF14], simplifying the expression to

$$R_L \approx \gamma np. \quad (1.10)$$

There are several assumptions on which the Langevin rate is based and which might not hold in case of organic semiconductors. Its validity can be verified by performing kinetic Monte Carlo simulations on lattices, as discussed in Section 1.6.2.

The overall recombination rate, $R_{\text{SRH}} + R_{\text{L}}$, enters the continuity equation (1.1). Experimentally the prevailing recombination mechanism can be probed by means of the classical Shockley diode equation with an ideality factor η , that differs depending on the dominant mechanism [WB14, LLY⁺14].

1.3.3 Excitons

The generation, transport, and decay of excitons can be described with a phenomenological equation for the population of excitons S_i , where i denotes the exciton type (triplet, singlet) [RKP⁺11]

$$\frac{\partial S_i}{\partial t} = G_i R(n, p) + \vec{\nabla} \cdot \vec{J}_i - \left(k_i^{(r)} + k_i^{(n)} \right) S_i - k_i^{(a)} f S_i^2 + \sum_{j=S,T} (k_{ji} S_j - k_{ij} S_i) - k_{\text{TPQ}}(n + p). \quad (1.11)$$

Here G_i is the exciton generation efficiency: for singlet excitons $G_S = 0.25$, while for triplet excitons $G_T = 0.75$. $k^{(r)}$ and $k^{(n)}$ are the radiative and non-radiative (position-dependent) decay rates, $k^{(a)}$ is the annihilation rate. The factor f is 0.5 if only one triplet is lost or 1 if both are lost. The radiative decay rate can be calculated using the dipole emission model [RKP⁺11, CPS78]. The exciton energy transfer rate, k_{ij} , describes the conversion of triplet excitons to singlets and vice versa. k_{TPQ} is the triplet-polaron quenching rate [RWL07] (assumed here to be the same for electrons and holes). Since excitons are charge-neutral, their transport is purely diffusive, i.e., $\vec{J}_i = D_i \vec{\nabla} S_i$. Note that the exciton dissociation into an electron and a hole has been neglected in Equation 1.11.

1.3.4 Boundary conditions and numerical solution

Equations (1.1)–(1.11) are complemented by the boundary conditions for the electrostatic potential, ψ , by setting the potential difference at the boundaries to $\psi_{\text{eff}} = V_{\text{app}} - V_{\text{int}}$, where V_{app} is the applied potential and V_{int} the built-in potential, defined as the difference of the materials' work functions.

The set of Equations (1.1)–(1.11) is normally solved using iterative schemes, until self-consistency for the electrostatic potential, density, and current is reached. The Gummel iteration method [Gum64] with a discretization according to a scheme proposed by Scharfetter and Gummel [SG69] can be used to solve linearized equations. This method is less sensitive to the initial guess than a Newton algorithm and thus is the method of choice despite its slower convergence in terms of iteration steps [KR11].

1.3.5 Limitations

Field, temperature, and charge density dependencies of the mobility entering drift–diffusion equations are normally parametrized in equilibrium or under stationary conditions. These dependencies can in general not be used to describe non-equilibrium, time-dependent processes. For example, charge-carrier relaxation makes the mobility effectively time-dependent, as it is evident from, e.g., impedance and dark-injection studies (see Section 1.12.2). Moreover, it has been shown that the current density in the device can be spatially inhomogeneous in all three dimensions (filamentary structures) [TBB04, MPC⁺06, RPT07], which then questions the applicability of mean-field descriptions. Lastly, some processes, for example exciton–electron interactions or energetic barriers between organic layers, are difficult to incorporate into drift–diffusion equations. The master equation, which we review in the next section, allows to consider the individual rates between charge transfer and other events. In the subsequent section we describe the Monte Carlo technique, that also allows to include excitonic processes.

1.4 Master equation

In inorganic, crystalline semiconductors charges are delocalized and energy eigenvalues of the electronic Hamiltonian form smooth bands. Consequently, one deals with band-like charge transport, where mobility decreases with increasing temperature. Contrarily, in amorphous organic semiconductors molecules are weakly bound by van der Waals and, consequently, intermolecular electronic couplings are small. As a result, excess electrons are localized on single molecules or their fragments. Moreover, orientational and positional *energetic* disorder helps to further localize charged excitations. In this situation, charge transport can be modeled as thermally-activated charge *hopping* between neighboring molecules. Mathematically, this is described by a Poisson process: The probability of an event to happen depends only on the time interval (no memory) and events do not occur simultaneously. The corresponding master equation, which describes the time evolution of a system with a discrete set of states i , then reads

$$\frac{dP_i(t)}{dt} = \sum_{j \neq i} [w_{ij}P_i(t) - w_{ji}P_j(t)], \quad (1.12)$$

where $P_i(t)$ is the probability to find the system in state i at time t and w_{ij} is the transition rate from state i to j . In most situations, the dimension of the state space is too large to use direct numerical differential equation solvers to solve for P_i . In special cases, e.g. for single charge carrier transport or transport of many carriers in a mean-field approximation, this equation can be rewritten in terms of site occupation probabilities, p_i .

1.4.1 Single-carrier charge transport

If only one charge carrier is present in the system, the state of the system is fully determined by the position of the charge, or the index of the molecule which this charge occupies. In this situation the occupation probability of the system state, P_i is equivalent to the site (molecule) occupation probability, p_i . The rates for transitions between states are then given by charge transfer rates, ω_{ij} (see section 1.6) and the master equation can be rewritten in terms of site occupation probabilities

$$\frac{dp_i(t)}{dt} = \sum_{j \neq i} [\omega_{ij}p_i(t) - \omega_{ji}p_j(t)]. \quad (1.13)$$

Equation (1.13) is a linear set of equations of size N , where N is the number of molecules in the system. It can be solved using standard numerical differential equation solvers [Hon90]. In special cases, e.g. for one-dimensional charge transport, it is even possible to obtain an analytic solution [Der83, ST01, Bar14]. Alternatively, one can use the kinetic Monte Carlo (KMC) algorithm, which is discussed in section 1.5.

1.4.2 Finite charge-carrier densities

In experimentally relevant conditions, charge densities have finite values. The system state is now given by a vector of indices of occupied molecules and the number of states increases dramatically. It is, however, still possible to reformulate the master equation (1.12) in terms of site occupation probabilities by using a mean field approximation [CB06, RLM⁺11]. The master equation then reads

$$\frac{dp_i}{dt} = \sum_{j \neq i} [\omega_{ij}p_i(1 - p_j) - \omega_{ji}p_j(1 - p_i)]. \quad (1.14)$$

The resulting equation is no longer linear in p_i and thus requires more involved numerical solvers. In most cases where one deals with many carriers the KMC method (see section 1.5) becomes

more practical: it does not rely on the mean field approximation but solves the original master equation, and it can easily be extended to other processes, such as exciton transport, triplet-triplet annihilation, etc.

1.4.3 Mobility and diffusion constant

The stationary solution of the master equation for a system in an external field \vec{F} allows to evaluate both charge carrier mobility and diffusion constant. For single-carrier transport, the mobility tensor $\hat{\mu} = \vec{v} \otimes \vec{F}/F^2$ reads

$$\mu_{\alpha\beta} = F^{-2} \sum_{ij} \omega_{ij} p_i r_{ij,\alpha} F_\beta, \quad (1.15)$$

where $r_{ij,\alpha} = r_{i,\alpha} - r_{j,\alpha}$ and \vec{v} is the average velocity of a charge carrier [RLM⁺11]. For finite charge carrier density $\rho = N/V$, where N is the number of carriers and V is the volume of the box, Equation 1.15 takes form

$$\mu_{\alpha\beta} = \frac{1}{\rho F^2 V} \sum_{ij} \omega_{ij} p_i (1 - p_j) r_{ij,\alpha} F_\beta. \quad (1.16)$$

In a similar fashion, occupation probabilities can be used to calculate charge and current distributions in the system [RLM⁺11]. Alternatively, one can directly analyze charge trajectories of kinetic Monte Carlo simulations and evaluate mobility tensor as

$$\hat{\mu} = \frac{\langle \vec{v} \rangle \otimes \vec{F}}{F^2}, \quad \text{with} \quad \langle \vec{v} \rangle = \frac{\Delta \vec{r}}{\Delta t}. \quad (1.17)$$

Here \vec{F} is the external electric field, \vec{r} is the charge position, Δt is the simulation time. The diffusion tensor can also be calculated directly from the charge trajectory generated without applied external field [HBR13]

$$D_{\alpha\beta} = \frac{\langle \Delta r_\alpha \Delta r_\beta \rangle}{2\tau}, \quad (1.18)$$

where $\Delta r_\alpha(t) = r_\alpha(t + \tau) - r_\alpha(\tau)$, or obtained from charge mobility with the help of the generalized Einstein relation, Eqn. (1.7).

1.5 Kinetic Monte Carlo

As we saw in the previous section, rewriting the master equation (1.12) to a form tractable for large systems (i.e. in terms of site occupation probabilities) requires certain approximations. Moreover, this step becomes less and less straightforward if events other than charge transfer are included, e.g., electron-hole recombination, exciton splitting, exciton decay or transfer. For these reasons, a different way of solving the master equation becomes more practical. Here, system dynamics, or trajectories in the phase space, or Markov chains, are generated explicitly by using so-called kinetic Monte Carlo (KMC) method.

KMC, also known as dynamic Monte Carlo, Gillespie algorithm, residence-time algorithm, n -fold way, or Botz-Kalos-Lebowitz algorithm, was initially developed by Doob [Doo42, Doo45]. The time update as it is used here was first introduced by Young and Elcock [YE66]. Bortz, Kalos and Lebowitz developed the same algorithm independently and applied it to the Ising model [BKL75]. Gillespie provided a physics-based derivation of the algorithm [Gil76, Gil77], which was then improved in terms of computational efficiency by Fichthorn [FW91] and Jansen [Jan95]. The version we will describe here is known as a variable step size method (VSSM) [Jan95].

1.5.1 Variable step size method

The variable step size method (VSSM) allows to group certain events and treat the groups and events in the group hierarchically. In case of charge transport with multiple charge carriers, for example, a two-level approach can be used. First, a charge is selected with the probability proportional to its *escape rate* ω_i , that is the sum of the rates of all possible moves of this charge away from the occupied site

$$\omega_i = \sum_{j=1}^m \omega_{ij}, \quad (1.19)$$

where m is the coordination number, i.e., the number of neighbors to which the site is connected and ω_{ij} are rates for all possible moves to connected sites. Afterwards, the destination site is chosen with a probability ω_{ij}/ω_i . Since we are dealing with a Poisson process, waiting times are exponentially distributed with a parameter λ that is the sum of all escape rates

$$\Delta t \sim \exp(\lambda), \quad \lambda = \left(\sum_i \omega_i \right)^{-1}. \quad (1.20)$$

In order to reproduce this distribution, the time in the VSSM algorithm is updated after each move with Δt drawn from an exponential distribution. In practice, this is achieved by drawing a random number u from a uniform distribution on the interval $(0, 1]$ and setting Δt to

$$\Delta t = -\lambda \ln(u), \quad u \sim \mathcal{U}((0, 1]). \quad (1.21)$$

1.5.2 Forbidden events

The VSSM algorithm can be adapted to efficiently treat forbidden events [Jan95]. In case of charge transport, for example, each site (molecule) can be occupied by one charge carrier at a time (Pauli exclusion principle). As a result, charge carriers obey Fermi–Dirac occupation statistics (see Section 1.3). Hence, if site j is already occupied, all incoming rates, $\omega_{i \rightarrow j}$ should be set to zero. This is computationally inefficient, since all rates (as well as escape rates) must be updated after every event. A much more efficient way is to keep the forbidden event in the event list. Once this event is attempted, i.e., a carrier attempts to hop to an occupied site, this destination site is marked as forbidden and another destination is selected from the remaining possibilities. If all surrounding sites are occupied, the algorithm switches to the level above, i.e., a different charge is selected and the previous one is added to a temporary list of forbidden events. The time is updated regardless of whether or not the event is forbidden or not (the charge moved or not). One can show that this strategy results in the same statistics as *a priori* removing all forbidden events from the event list [Jan95].

1.5.3 Efficiency and parallelization

Developing an efficient kinetic Monte Carlo code for charge/exciton transport is a rather challenging task. Indeed, if only the Pauli exclusion principle is taken into account, a single charge transfer event does not affect the rates, only the (local) list of forbidden events should be updated. Hence, all rates can be precomputed before the KMC simulation is performed. If (long-range) Coulomb interactions are included, every charge transfer event changes all rates. In other words, energy differences between two states of the system depend now on the relative positions of all charges in the system. To avoid updating rates at every KMC step, one can use scale-separation techniques: since mesoscopic charge densities evolve on timescales much longer than typical charge transfer times, electrostatic fields created by far-off charges can be treated in a mean-field way,

e.g. by solving the Poisson equation. In this case, one can update local rates at every step, while all rates are updated only every 100 to 1000 steps [KvdHAH⁺15].

Even the local rate updates can become computationally costly for systems with many charge carriers. In this situation, the binary tree search algorithm helps to improve computational efficiency by providing a faster way of identifying which events and escape rates should be updated. By using this algorithm one can gain a factor of 10 speedup for systems with 10% occupied sites [KvdHAH⁺15]. Another alternative is to use the next reaction method [GB00], an improved version of the first reaction method, where a dependency graph is used to determine which rates to update.

Apart from trivial parallelization, where multiple copies of the system with different initial conditions are run in parallel, Monte Carlo schemes can be parallelized by dividing the simulation volume into sub-volumes treated as individual simulations [Lub88, SA05, MF07, MMKP08]. An efficient parallel implementation on GPUs has also been demonstrated [vdKK16].

1.6 Rates

To parametrize the master equation (1.12), we need to evaluate the rates of all elementary processes of interest. For example, for charge transport, charge transfer rates must be evaluated for all neighboring molecular pairs. To make this computationally feasible, we often rely on simplified theoretical treatments of transfer reactions. In this section we review several of such theories as well as introduce the corresponding rate expressions.

1.6.1 Charge transfer

The simplest expression for the charge transfer rate, proposed by Miller and Abrahams [MA60], is the rate of thermally activated, barrierless tunneling between two localized electronic states. The corresponding rate is proportional to the Boltzmann prefactor of the free energy difference between the initial and final states, ΔE_{ij} , and the electronic overlap between the states, which decays exponentially with the molecular separation

$$\omega_{ij} = \begin{cases} \omega_0 \exp(-2\gamma r_{ij}) \exp\left(-\frac{\Delta E_{ij}}{k_B T}\right) & \Delta E_{ij} > 0, \\ 1, & \Delta E_{ij} \leq 0, \end{cases} \quad (1.22)$$

where $1/\gamma$ is the localization length of the charge, r_{ij} is the distance between the two molecules, and ω_0 is the attempt frequency. The simplicity and intuitiveness of this rate justified its use at early stages of understanding of charge transport in organic semiconductors [Bae93].

Environmental effects, as well as molecular reorganization upon charging/discharging (i.e., the energetic barrier between the initial and final states) have been accounted for in the so-called Marcus charge transfer rate [Mar93, HRM05]

$$\omega_{ij} = \frac{2\pi}{\hbar} \frac{J_{ij}^2}{\sqrt{4\pi\lambda_{ij}k_B T}} \exp\left[-\frac{(\Delta E_{ij} - \lambda_{ij})^2}{4\lambda_{ij}k_B T}\right]. \quad (1.23)$$

Again, $\Delta E_{ij} = E_i - E_j$ is the driving force, or the free energy difference of the final and initial states of the charge transfer reaction [MK11]. An accurate evaluation of these energies using polarizable force-fields is discussed in Section 1.7. J_{ij} are electronic coupling elements. They are intimately related to the overlap of the diabatic electronic states, as discussed in Section 1.9. Finally, λ_{ij} is the sum of the external and internal reorganization energies, discussed in more detail in Section 1.8.

The main issue with the classical Marcus rate is that the intramolecular vibrational modes promoting the charge transfer reaction are energetically comparable to the C–C bond stretching mode at room temperature, $\hbar\omega_{CC} \sim 0.2 \text{ eV} \gg k_B T \sim 0.025 \text{ eV}$. Therefore, these modes

should be treated quantum mechanically. For a common set of intramolecular high-frequency (quantum-mechanical) and an outer sphere low-frequency (classical) vibrational coordinates, a mixed quantum-classical multi-channel generalization of the Marcus formula is readily available [BJ07, MK11]. A generalization for the bimolecular electron transfer rate with independent sets of coordinates for donor and acceptor has also been proposed [RLM⁺11].

Another rate expression has recently been proposed by Weiss and Dorsey [EMW94, FD85, GW85]. In the low temperature limit, $\hbar\nu_c/k_B T \gg 1$, it reads

$$\omega_{ij}(\epsilon) = \frac{J_{ij}^2}{\hbar^2 \nu_c} \left(\frac{\hbar \nu_c}{2\pi k_B T} \right)^{1-2\alpha} \frac{\left| \Gamma \left(\alpha + i \frac{\Delta E_{ij}}{2\pi k_B T} \right) \right|^2}{\Gamma(2\alpha)} \exp \left(\frac{\Delta E_{ij}}{2k_B T} - \frac{|\Delta E_{ij}|}{\hbar \nu_c} \right). \quad (1.24)$$

Here $\Gamma(z)$ is the Gamma function and ν_c is the characteristic frequency, or the largest frequency in the Ohmic bath, which is related to the reorganization energy, λ , by $\lambda = 2\alpha\hbar\nu_c$. The Kondo parameter, α , describes the coupling strength between the charge and the heat bath [LCD⁺87]. In the high temperature limit the Weiss–Dorsey rate simplifies to the Marcus rate. Indications that the Weiss–Dorsey rate is better suited for describing charge transport, especially at low temperatures and high fields, have recently been reported [AKC⁺13].

1.6.2 Electron–hole recombination

The microscopic process of electron–hole recombination is straightforward: whenever a hole and an electron occupy the same site (molecule), they recombine with a certain rate, w_r . Radiative recombination leads to a photon emission which is the basis of OLED functionality.

On a macroscopic level, electron–hole recombination is traditionally described by the Langevin equation (see Section 1.3.2), with a prefactor proportional to the sum of electron and hole mobilities. Extensive kinetic Monte Carlo simulations were performed to verify this dependency [vdHvOCB09]. An excellent agreement was found if the electron and hole mobilities are extracted from simulations with both carrier types, which was attributed to the change in mobilities upon inclusion of two carrier types due to their Coulomb attraction. Deviations at high charge concentrations ($> 10^{-3}$ carriers per molecule) were also observed: here, the average electron–hole distance becomes smaller than the thermal capture radius, $r_c = e^2/4\pi\epsilon\epsilon_0 k_B T$, violating assumptions used in the derivation of the Langevin formula.

1.6.3 Energy transfer

We now briefly review rate expressions used to describe electronic excitation (energy) transfer (EET). Electronic energy transfer is also known as a resonant energy transfer (RET).

A theory explaining the mechanism of EET was first proposed by Förster [Foe48]. The electronic interaction promoting EET relies on a coupling of the donor and acceptor molecules via a Coulombic interaction. Similar to charge transfer, Förster theory relies on the Fermi’s Golden Rule with the electronic coupling between donor and acceptor treated perturbatively. Additional assumptions are that the system equilibrates after the electronic excitation of the donor on a timescale much faster than that of EET and that coupling to the bath (given by the absorption line shape) is much greater than the electronic coupling between donor and acceptor. Energy conservation in the weak coupling limit results in a coupling element which is proportional to overlap of the donor fluorescence spectrum with the acceptor absorption spectrum. The spectral overlap includes nuclear overlap (in the form of Franck-Condon factors) which depends on the spectral line shapes and thus provides the temperature dependence of the EET rate. Under these

assumptions the EET rate between emitters i (donor) and j (acceptor) takes a simple form

$$\omega_{ij}^{\text{F}} = \frac{1}{\tau_{r,i}} \left(\frac{R_{\text{F},ij}}{r_{ij}} \right)^6, \quad (1.25)$$

where $\tau_{r,i}$ is the radiative life time of the emitter (donor), r_{ij} is the separation between donor and acceptor, $R_{\text{F},ij}$ is the Förster radius for transfer from donor to acceptor.

EET process can occur even when the Coulomb-term-mediated electronic transitions are forbidden. Dexter provided a derivation for the case when the Coulombic interaction is negligible and EET is due to the exchange part [Dex53]. This rate decays exponentially with intermolecular separation

$$\omega_{ij}^{\text{D}} = k_{\text{D}} \exp(-2\gamma r_{ij}), \quad (1.26)$$

where $1/\gamma$ is the wavefunction decay length and k_{D} is the Dexter prefactor proportional to the exchange integral.

Note that since the exchange integral is a quantum mechanical correction to the Coulombic repulsion, the total EET rate is always a sum of the two rates. However, due to the exponential decay of the Dexter coupling, the electronic interaction that mediates EET at separations greater than 5 Å is invariably Coulombic.

The importance of exchange and other short-range interactions, as well as higher multipole contributions to the Coulombic interaction, have been examined fairly extensively, helping to improve the accuracy of rate expressions (1.25) and (1.26). An overview of these extensions can be found in Refs. [SG94, SHG95, HSG94, Spe96, FPZE08].

1.7 Density of states

In the previous section we saw that charge transfer rates depend on the energies of the initial and final states of the charge transfer complex. In an amorphous organic semiconductor every molecule is embedded in a unique environment and therefore every molecule has its unique set of energy levels, electron affinity, and ionization potential. The set energy levels available for an excess charge is termed as the density of states (DOS). In this section we discuss several methods of evaluation of the DOS of an amorphous organic semiconductor.

1.7.1 Gaussian disorder

The simplest approach to model the DOS of organic semiconductor is to assume a Gaussian distribution of energy levels

$$g(E) = \frac{1}{\sqrt{2\pi\sigma^2}} \exp \left[-\frac{(E - \bar{E})^2}{2\sigma^2} \right]. \quad (1.27)$$

This phenomenological expression, first proposed by Bäessler [Bae93] and termed the Gaussian disorder model (GDM), is motivated as follows: randomly oriented dipole moments in an amorphous material interact with each other, thus influencing the energy levels of neighboring molecules. As a result of the central limit theorem, this leads to approximately Gaussian distributed energy levels. The width of the distribution, σ , is called the *energetic disorder* and can be extracted from temperature-dependent mobility measurements [TBdLM04, LH07] or from simulations, as discussed in Section 1.11.1.

The original model was extended to the correlated disorder model (CDM) by accounting for spatial correlations that arise from the dipole interaction of neighboring molecules [NDK⁺98].

For randomly oriented dipoles, \vec{p}_j , the the electrostatic energy of a site i is given by [DPK96]

$$E_i = -\frac{q}{4\epsilon} \sum_{j \neq i} \frac{q\vec{p}_j \cdot (\vec{r}_j - \vec{r}_i)}{|\vec{r}_j - \vec{r}_i|^3}, \quad (1.28)$$

where ϵ is the dielectric permittivity and q is the charge. In case of equal absolute values, $|\vec{p}_j| = p$, and dipoles fixed on a cubic lattice with lattice constant a , the sum can be evaluated using Ewald summation [dLPS80, Ewa21], yielding a Gaussian DOS with energetic disorder $\sigma = 2.35 qp/\epsilon a^2$ [You95, NDK⁺98]. The spatial energy correlation function

$$\kappa(r) = \frac{\mathbb{E}[(E(\vec{r}_i) - \bar{E})(E(\vec{r}_j) - \bar{E})]}{\sigma^2} \quad (1.29)$$

is then given by $\kappa(r) \approx 0.74 \frac{a}{r}$ [NV95]. Here $r = |\vec{r}_i - \vec{r}_j|$ is the distance between two molecules, \bar{E} is the mean of the energy distribution and $\mathbb{E}[\cdot]$ is the expectation value. Note that the spatial correlation function of this simple model system depends only on the lattice spacing a , limiting its applicability to realistic morphologies [KA16], as discussed in Section 1.11.1.

The Gaussian density of states is at the heart of the family of Gaussian disorder models (GDM), where Miller–Abrahams rates, Equation 1.22, with the Gaussian density of states are assumed for a charge hopping on a cubic lattice. Extensive kinetic Monte Carlo simulations of these models helped to parametrize the mobility as a function of temperature, field and field carrier density [Bae93]. It was extended by including the important influence of charge carrier density in the extended Gaussian disorder model (EGDM) [PCT⁺05] without spatial correlation of site energies. The mobility expression in the EGDM at finite can be written as a product of three functions,

$$\mu(T, F, \rho) = \mu_0(T)g(T, \rho)f(T, F), \quad (1.30)$$

where

$$\begin{aligned} \mu_0(T) &= 1.8 \times 10^{-9} \mu_0 \exp[-C\hat{\sigma}^2], & g(T, \rho) &= \exp\left[\frac{1}{2}(\hat{\sigma}^2 - \hat{\sigma})(2\rho a^3)^\delta\right], \\ f(T, F) &= \exp\left[0.44(\hat{\sigma}^{3/2} - 2.2)\left(\sqrt{1 + 0.8\hat{F}^2} - 1\right)\right], & \delta &= 2\frac{\ln(\hat{\sigma}^2 - \hat{\sigma}) - \ln(\ln 4)}{\hat{\sigma}^2}, \end{aligned} \quad (1.31)$$

with $C = 0.42$, $\hat{F} = eaF/\sigma$ and $\hat{\sigma} = \sigma/k_B T$. A similar parametrization, termed extended correlated disorder model (ECDM), also exists for the spatially correlated DOS [BMBC09].

1.7.2 Perturbative approach

While Gaussian disorder models have been successful in describing many properties of organic semiconductors, they do not provide a direct link to the material morphology or chemical composition. A perturbative approach allows to evaluate site energies in atomistically-resolved (see Section 1.10), large-scale morphologies. Furthermore, it can also be used to parametrize Gaussian disorder models and perform large-scale simulations (see Section 1.11.2).

For every molecular pair, our quantity of interest is the energy difference $\Delta E_{ij} = E_i - E_j$, which is the energy separation between the minima of the diabatic potential energy surfaces. In systems with weak intermolecular couplings, one can treat interactions with the environment perturbatively: the intermolecular electrostatic and induction contributions are then given by the first- and second-order terms in the expansion of the interaction energy [Sto97].

The total energy of an ion embedded in a molecular environment thus includes an internal contribution E_i^{int} , i.e., the electron affinities for electrons and ionization potentials for

holes of *isolated* molecules. These can vary from one molecular pair to another because of different energy levels for different types of molecules, or different conformers of the same molecule. Correspondingly, the *external* contribution is due to the electrostatic and induction interactions, E_i^{el} and E_i^{ind} , of a charged molecule with the environment. These interaction energies are determined by the electrical charge distribution and the polarizability distribution, respectively, in the environment of the charged molecule. Overall, the total energy of molecule i is then given by

$$E_i = E_i^{\text{int}} + E_i^{\text{el}} + E_i^{\text{ind}}. \quad (1.32)$$

Most difficult to evaluate is the interaction with the environment. This is for two reasons: First, the underlying interactions are long-ranged and thus large system sizes are needed to converge the values of site energies. Second, special summation techniques are needed in order to evaluate interactions of an ion with a neutral *periodic* environment [PA16, PTE⁺14, PA15, And14]. Also note that the perturbative evaluation of site energies relies on accurate molecular representations in terms of distributed multipoles and polarizabilities and is computationally demanding, in spite of being classical [Tho81].

1.7.3 Hybrid approaches

Using Equation (1.32), the site energies can be evaluated by solving a microscopic analogue of the Poisson equation. The self-consistent solution is normally achieved using iterative schemes for induced multipoles and Ewald summation techniques for static multipoles, which is computationally demanding. The role of hybrid schemes is to reduce computational cost. Here, one relies on the fact that the fields created by the far-off charges can be treated in a mean-field way, i.e., obtained by solving the Poisson equation. Nearest-neighbor interactions (i.e., interactions between molecular pairs within a certain cutoff distance) are still evaluated explicitly. This scheme also allows to add metallic electrodes as image charges and has been used extensively to simulate multilayered OLED devices [vMC08b, vdHUR⁺09, CB12]. To improve computational efficiency, in this approach all induction interactions are taken into account effectively, by re-scaling interaction energies by the (effective) dielectric constant of the medium.

1.8 Reorganization energy

The reorganization energy, responsible for the energy barrier between diabatic states as well as for the broadening of energy levels of the electron detachment/attachment spectra, has two contributions. The *internal* reorganization energy is a measure for how much the geometry of the charge transfer complex adapts while the charge is transferred. It can be estimated based on four points on the diabatic potential energy surfaces (PES) [BBCC04, RLM⁺11]

$$\lambda_{ij}^{\text{int}} = E_i^{nC} - E_i^{nN} + E_j^{cN} - E_j^{cC}. \quad (1.33)$$

Here, small letter denotes the state and capital letter the geometry of a molecule, e.g., E_i^{nC} is the internal energy of the molecule i in the geometry of its charged state. Treatments which do not approximate the PES in terms of a single shared normal mode are also available [Rei01, RLM⁺11, MK11].

An additional contribution to the overall reorganization energy results from the rearrangement of the environment in which the charge transfer takes place. In a classical case, this outer-sphere reorganization energy, λ^{out} , contributes to the exponent in the rate expression in the same way as its internal counterpart. Assuming that charge transfer is significantly slower than electronic polarization but much faster than the nuclear rearrangement of the environment, λ^{out} can be evaluated from the electric displacement fields created by the charge transfer complex [MK11], provided that the Pekar factor is known. Alternatively, one can use polarizable

force-fields [MT10] or QM/MM methods [NB08]. It also turns out that the classical Marcus expression for the outersphere reorganization energy (inversely proportional to the molecular separation) can predict negative values of λ^{out} for small intramolecular separations, which is unphysical and hence should be used with care [RLM⁺11].

1.9 Electronic coupling elements

Electronic coupling elements, or transfer integrals, J_{ij} , entering the charge transfer rate equations (1.23) and (1.24) are off-diagonal matrix elements, $J_{ij} = \langle \psi_i | \hat{H}^{\text{el}} | \psi_j \rangle$, of the electronic Hamiltonian, $\hat{H}^{\text{el}} = \hat{T}^{\text{el}} + \hat{V}^{\text{el-el}} + \hat{V}^{\text{nuc-el}}$, in the basis of diabatic (non-interacting) states, ψ_i [MK11]. A number of approaches can be used to evaluate electronic coupling elements. Their efficiency and accuracy depends on how the diabatic states and Hamiltonian are constructed, as well as how the matrix projection is performed.

Diabatic states are often approximated by the highest occupied molecular orbital (HOMO) of monomers for hole transport, or the lowest unoccupied molecular orbital (LUMO) for electron transport (“frozen core” approximation) [BKA10, HK05, VCdSF⁺06]. An approximate diabatic basis can also be constructed using constrained density functional theory [VVKK⁺10].

The dimer Hamiltonian can be constructed using semi-empirical methods, e.g. the ZINDO Hamiltonian [RZ73, Kir08, BBCC04, CCdSF⁺07]. This approach does not require a self-consistent evaluation of the dimer Hamiltonian and is therefore computationally very efficient [Kir08]. One can also employ the density functional theory and use either the fully-converged Hamiltonian or only the initial guess [BKA10]. Another way to improve the efficiency is to reduce the number of orbitals for which electronic couplings are calculated. A detailed comparison of accuracy and efficiency of different approaches can be found in Refs. [BKA10, KHH⁺14, GVH⁺14].

For (approximately) spherically-shaped molecules the logarithm of the squared electronic coupling, $\log(J_{ij}^2)$, decays linearly as a function of the intermolecular separation r (at least for large distances), justifying the functional form of the Miller-Abrahams rate, see Equation (1.22). If molecular pairs are extracted from the respective dimers in the realistic atomistic morphology, $\log(J_{ij}^2)$ is often Gaussian distributed, with a mean and variance that depend on the molecular separation [KSB⁺14, KvdHAH⁺15]. This observation can be used to parametrize coarse-grained (stochastic) charge transport models, as discussed in Section 1.11.1.

Since electronic couplings are related to the overlap of electronic orbitals participating in charge transport, they are very sensitive to the relative positions and orientations of molecules. Hence, an amorphous morphology of an organic material should be generated as precisely as possible. The corresponding methods are covered in the next section.

1.10 Morphology

In the previous sections we explained how charge/exciton transport and recombination can be mapped on a series of events with specified rates. We have also emphasized that rates are very sensitive to both local and global molecular ordering. For computer-based predictions of material properties it is therefore important to simulate material morphology as realistically as possible. In OLEDs, we usually deal with *amorphous* molecular arrangements – crystalline films are often less efficient in OLEDs because of the resulting large exciton diffusion distances, leading to enhanced exciton loss due to quenching processes. Amorphous films have a well-defined local structure which depends on molecular interactions and processing conditions. In this section we describe how amorphous morphologies of $10^4 - 10^5$ molecules can be simulated using atomistic force fields or coarse-grained models. These systems can then be used to study small-scale charge transport [AKM⁺07, KMN⁺07, NKKF09, RLM⁺11, NL08, FSM⁺12], or to

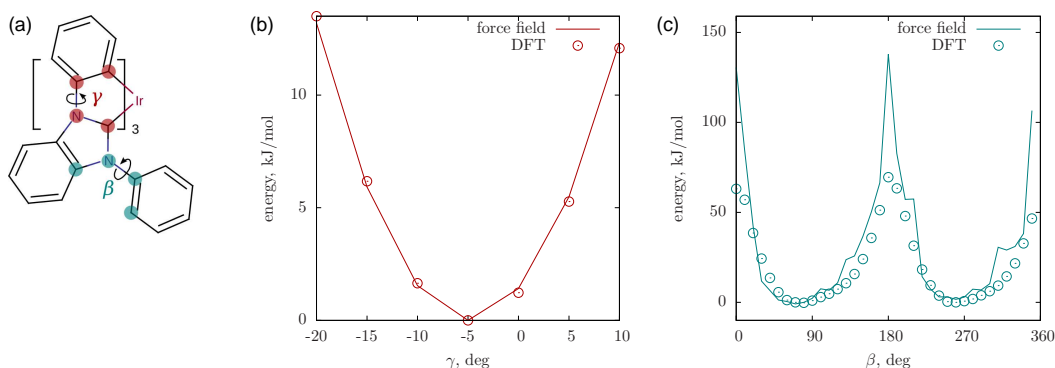


FIGURE 1.3 Potential energy scans of two dihedral angles of the DPBIC molecule, the chemical structure of which together with the definition of dihedral angles is shown in the inset (a). Symbols show DFT energies (B3LYP/6-311g(d,p)) and lines the force-field energies after adjusting the force field parameters. Reproduced with permission from Adv. Funct. Mater, 2015, 25, pp 1955–1971.

parameterize mesoscale models, as discussed in Section 1.11.1.

1.10.1 Classical force fields

The role of classical force fields in simulation of organic semiconductors is two-fold. First, they are used to generate atomistically-resolved morphologies of molecular assemblies. Second, they are employed to evaluate the solid-state electrostatic and induction contributions to site energies (see Section 1.7). In both cases these classical molecular representations should be appropriately parametrized.

For site energy calculations it is important to evaluate electrostatic and induction contributions as accurately as possible. The corresponding parametrization is rather straightforward: a perturbative expansion of the intermolecular interaction energies is based on distributed multipoles (electrostatic interaction) and distributed polarizabilities (induction interaction) [Tho81, Sto85, Sto97, Sto05, MS06]. Van der Waals interactions are normally ignored since we are interested in free energy differences between charged and neutral states of the system. To improve computational efficiency, one can also use machine-learning techniques to devise simple structure-property relations for, e.g., atomic multipoles of molecular conformers [BAvL15].

Polarizable force fields based on distributed multipole expansions are still computationally prohibitive for simulating molecular arrangements of large systems. Moreover, parametrizations of effective *pairwise* potentials (partial charges and Lennard–Jones parameters), which mimic many-body van der Waals and induction interaction energies, are a non-trivial task which largely relies on experimental input [JTR88, JMTR96]. Standard forces fields, e.g. those suitable for bio-systems, are often not transferable to organic molecules with large π -conjugated subsystems. A representative example is the comparison of the Williams 99 and the OPLS force fields for the amorphous mesophase of Alq₃ [LLA09], which predict fairly different densities, radial distribution functions, and glass transition temperatures.

That being said, the development of new force fields for organics is currently limited to refitting of partial charges using the Merz–Singh–Kollman [BMK90] scheme or the CHELPG [BW90] scheme, and a parametrization of missing bonded interactions from first-principles scans (see Figure 1.3). The remaining parameters are often taken from standard force fields, such as OPLS [JTR88]. Reparametrized force fields are then verified against experimentally available densities and glass transition temperatures.

1.10.2 Morphology simulations

With the force field at hand, one can, in principle, simulate amorphous molecular assemblies. For systems with periodic boundaries in all directions this is done by first equilibrating the system above the glass transition temperature and then quenching it to room temperature in the *NPT* ensemble using molecular dynamics [MAHB⁺12, LA10, LLA09].

For thin slabs (2D-periodic systems) one can directly deposit molecules either using molecular dynamics [PTE⁺14] or Monte Carlo [NDLW13] techniques. In both cases the dynamics of deposition is not realistic. In other words, if surface diffusion plays an important role (e.g., in case of guest aggregation in the host) these techniques cannot be applied in a straightforward manner, since the length scales and time scales required of host aggregation cannot be reached by atomistic molecular dynamics simulations. It is, however, possible to explore the fact that certain parts of molecules evolve on much slower time scales and larger length scales and to combine several coherently moving atoms, connected via stiff degrees of freedom (e.g., bonds) into a single interaction site, as it is done, for example, in the united atom force-fields with hydrogens incorporated into heavier atoms [MSSG⁺15]. By doing this, we reduce the number of degrees of freedom to be propagated and, more importantly, obtain a much smoother potential energy landscape in terms of the *coarse-grained* degrees of freedom [vLTRS04] (softer interaction potentials, less friction), allowing one to simulate ten to hundred longer times and system sizes [MSSG⁺15].

In order to perform correct statistical sampling of the coarse-grained degrees of freedom, the potential of mean force should be used as the interaction potential [NCA⁺08], which is inherently a many-body potential. To reduce computational cost, this potential is represented as sum of a few functions, i.e., projected onto the basis functions of the force field. The accuracy of the coarse-grained model thus becomes sensitive to the way the projection is performed as well as the number of basis functions that are used to represent the coarse-grained force-field [R.JL⁺09]. Existing projection schemes either try to reproduce various pair distribution functions (structure-based coarse-graining [Sop96, LL95, RPMP03, JAKP12]), to match the forces [EA94, IPBV04, NCA⁺08], to minimize the information loss in terms of relative entropy [She08], or to use liquid state theory [NCAV07]. An extensive overview of such coarse-graining techniques is provided in Ref. [Noi13]. Often, the accuracy of the coarse-grained model can be improved by explicitly incorporating information about macroscopic properties of the system, i.e., its equation of state or the symmetry of its mesophase [DM10, GPK⁺13, PDTA14]. Moreover, one can further reduce the number of degrees of freedom by introducing anisotropic interaction potentials. Eventually, atomistic details can be re-introduced into coarse-grained morphologies [GPK⁺15].

1.11 Scale bridging

Now that we have seen how an OLED device can be modeled on different time and length scales, we eventually would like to transfer our knowledge about the system between the scales. For example, drift–diffusion equations (Section 1.3) can be used to calculate current–voltage curves of a device (micrometer scale). However, they require expressions for charge carrier mobility, the diffusion constant and, in case recombination is taken into account, the recombination rate, all as a function of external field, carrier density, and temperature. Microscopic simulations (see Sections 1.4–1.10) can provide this information, at the same time retaining the link to the molecular structure. However, they are becoming computationally too demanding for high charge densities and large systems sizes required to parametrize these dependencies. Our aim here is to provide several strategies which can be used to link different time and length scales.

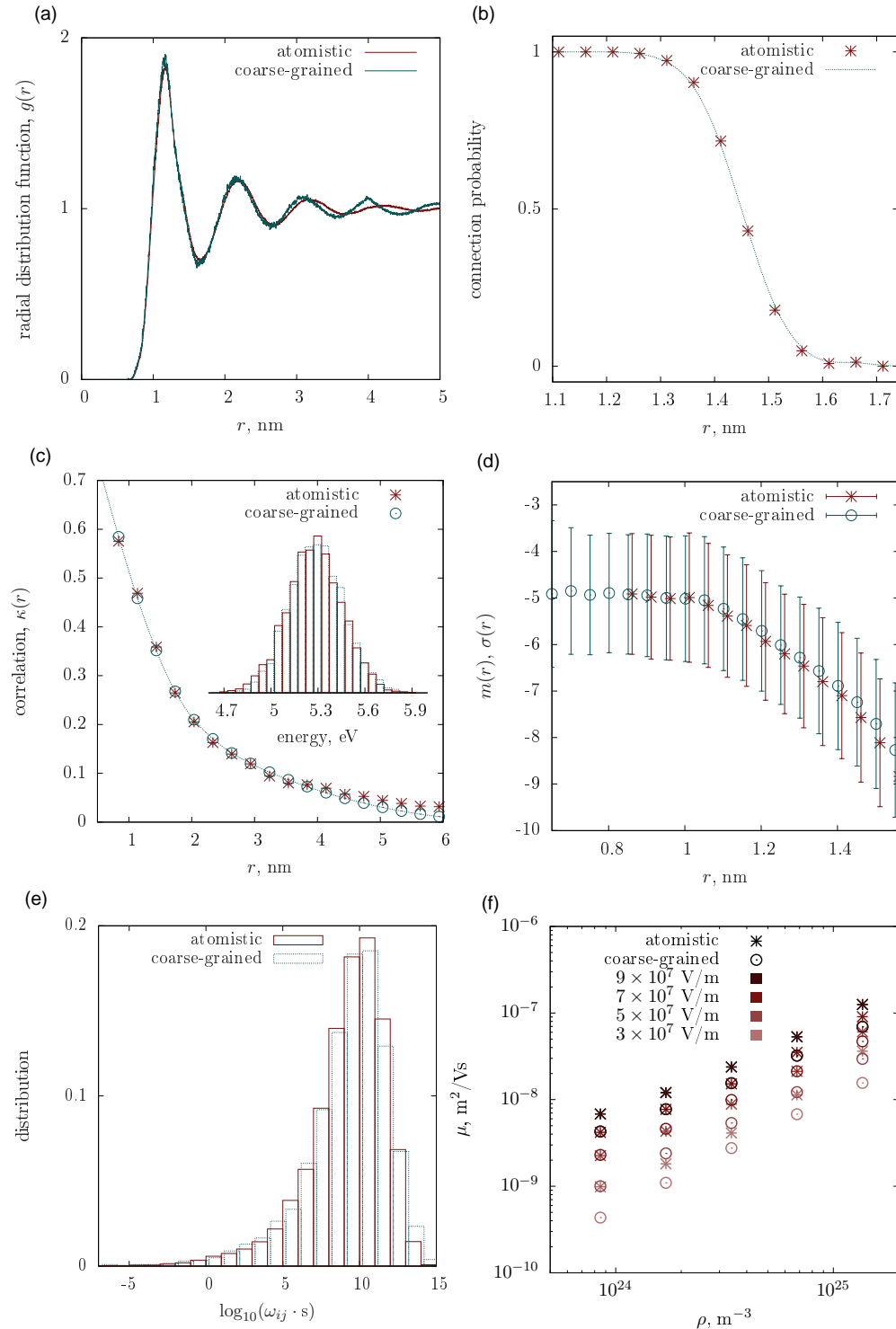


FIGURE 1.4 Comparison of hole states and hole mobilities in the atomistic reference system of DPBIC and in a stochastic model. (a) Radial distribution function, $g(r)$, where r is the center-of-mass distance. (b) Probability for sites to be connected. (c) Spatial correlation function, $\kappa(r)$, as defined in Equation (1.29); Inset: Site energy distribution with a mean (ionization potential) of 5.28 eV and an energetic disorder of $\sigma = 0.176$ eV. (d) Mean m and width σ of a distribution of the logarithm of squared electronic couplings, $\log_{10}(J^2/\text{eV}^2)$, for molecules at a fixed separation r . (e) Rate distributions. (f) Mobility as a function of hole density at different electric fields. Reproduced with permission from Adv. Funct. Mater, 2015, 25, pp 1955–1971.

1.11.1 Stochastic models

In an OLED, charges are inhomogeneously distributed [KSB⁺15] and charge density variations span several orders of magnitude. To cover the required density range in simulations, one needs to deal with relatively large systems – this quickly becomes computationally demanding if all rates are evaluated from first principles, as described in Section 1.6. To remedy the situation, one can devise a phenomenological algorithm to parametrize the master equation. In this section we outline how such an algorithm can be constructed for charge transport simulations.

We first note that the master equation (Section 1.4) is completely determined by the event rates. In case of charge transport, these rates depend on site energy differences, electronic coupling elements, and reorganization energies. In order to evaluate observables of interest (e.g. charge mobility), one additionally needs site positions. Hence, the algorithm should be able to reproduce (statistically) several distribution and correlation functions.

Let us start with molecular positions. In an amorphous solid, both positions and orientations are completely defined by a set of (many-body) spatial correlation functions. For (approximately) spherically-shaped molecules, the pair correlation function, or radial distribution function, $g(r)$, which quantifies the density of molecules at a separation r a molecule, contains the most relevant structural information. To reproduce this function approximately, one can use “thinning of a Poisson process” [BSP⁺12, KSB⁺14]. More accurate coarse-graining techniques, such as iterative Boltzmann inversion [TKB⁺98, RPMP03] or inverse Monte Carlo [LL95, Sop96, MBV⁺09], allow a (numerically) exact reproduction of the radial distribution function [KvdHAH⁺15]. These methods optimize a pair interaction potential, $U(r)$, in a way that the corresponding $g(r)$ is reproduced. These methods rely on the Henderson theorem [Hen74] which states that there is a unique correspondence between $U(r)$ and $g(r)$. An illustration of this algorithm for an amorphous layer of DPBIC is presented in Figure 1.4(a). The approach can also be applied to non-spherical molecules, by using several interacting sites per molecule [RJL⁺09].

The second ingredient of the stochastic model is the connectivity: in the atomistic model only molecules within a certain cutoff distance are used for calculating charge transfer rates. The rest of the rates is set to zero. This is justified by the fact that electronic coupling elements decrease roughly exponentially with molecular separation [KvdHAH⁺15] (see, e.g., Equation (1.22)). The distance that determines whether or not two molecules are connected is given by their two closest atoms. Since this information is not present in the coarse-grained model, the resulting probability of two sites to be connected, as a function of their center-of-mass separation, is given by corresponding probability extracted from the reference data. Figure 1.4(b) shows this probability for an amorphous DPBIC layer.

As explained in Section 1.7, the stochastic generation of site energies should reproduce both their distribution function (density of states) and their spatial correlation. This can be achieved by mixing in site energy contributions of neighboring sites [KA16]. Figure 1.4(c) shows the spatial correlation function for an amorphous DPBIC layer.

Electronic coupling elements can also be generated using appropriate distributions. These distributions are, however, separation-dependent: the logarithm of squared transfer integrals, $\log J^2$ (which is often Gaussian distributed) depends on molecular separation. For DPBIC, the distance dependence of the mean and the standard deviation is shown in Figure 1.4(d). In the stochastic model transfer integrals are then drawn from such distant-dependent distributions.

With all necessary rate ingredients, one can now validate the model, e.g., by evaluating the distribution of rates, see Figure 1.4(e), or by directly comparing charge carrier mobilities, as shown in Figure 1.4(f). Note that charge transport in systems with large energetic disorder has pronounced finite size effects [LA10]. Therefore, similar system sizes should be used to compare stochastic and reference simulations.

Since stochastic models are computationally significantly less demanding, they can serve as an intermediate step between atomistic and macroscopic (drift–diffusion) descriptions, as discussed

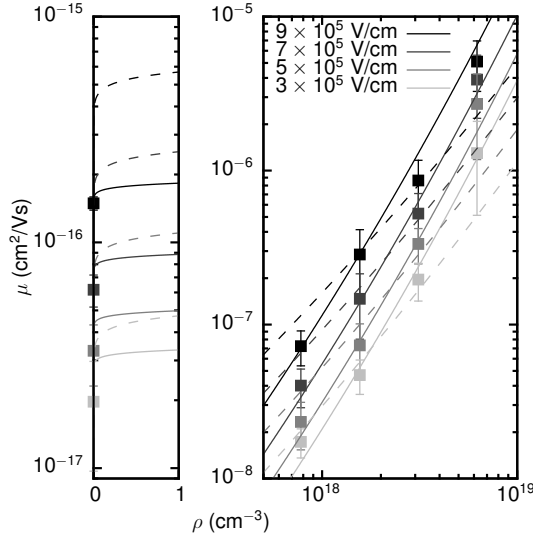


FIGURE 1.5 Parametrization of lattice models from simulated DCV4T hole mobilities, μ , for different hole densities, ρ . Symbols are the simulated values for four different external fields, solid lines are the fit to the EGDM and dashed lines the fit to the ECDM. An extrapolation has been used to obtain non-dispersive values (i.e., without finite-size effects) in the limit of zero density. Reprinted with permission from J. Chem. Theory Comput., 2014, 10, pp 2508–2513.

in the next section.

1.11.2 Parametrization of Gaussian disorder models

As mentioned in Section 1.3, macroscopic OLED modeling requires charge mobility as a function of external field, temperature, and carrier density, $\mu(T, F, \rho)$. Analytic expressions of these dependencies can be provided by the extended Gaussian disorder model (EGDM) and extended correlated disorder model (ECDM), as discussed in Section 1.7.1. These generic expressions include several material-specific parameters. In this section we describe how to determine these parameters from simulations of small systems.

Both EGDM and ECDM depend parametrically on the lattice constant a , the energetic disorder σ (see Section 1.7) and a prefactor μ_0 , which is related to the temperature-dependent mobility at zero field and charge density by $\mu_0(T) = 1.8 \times 10^{-9} \mu_0 \exp(-0.42\hat{\sigma}^2)$ for the EGDM (see Section 1.7.1) or $\mu_0(T) = 1.0 \times 10^{-9} \mu_0 \exp(-0.29\hat{\sigma}^2)$ in case of the ECDM.

In principle, both a and σ can be evaluated in a relatively small system: a as the mean distance between neighboring molecules and σ as the width of the DOS that results from perturbative energy calculations. μ_0 can be extracted from charge transport simulations performed at different temperatures. This approach, however, does not lead to reliable parameterizations [KSB⁺14, KvdHAH⁺15]. Indeed, a multidimensional fit of simulated mobilities to the EGDM or ECDM expressions, for a wide range of temperatures, charge densities, and external fields, yields a very different set of parameters. A comparison of these two approaches for amorphous dicyanovinyl-substituted quaterthiophe (DCV4T) and DPBIC is given in Table 1.1. One can see, for example, that the EGDM underestimates the energetic disorder, while the ECDM overestimates it. In both cases spatial site energy correlations are responsible for this discrepancy: EGDM does not include correlations and compensates for higher mobility values by reducing the energetic disorder σ . On the other hand, ECDM overestimates spatial correlations, and compensates this by reducing the lattice constant [KA16]. The discrepancy between microscopic values and fits

(a) DCV4T				(b) DPBIC			
	a [nm]	σ [eV]	$\mu_0(300\text{ K})$ [m^2/Vs]		a [nm]	σ [eV]	$\mu_0(300\text{ K})$ [m^2/Vs]
microscopic	0.86	0.253	2.0×10^{-21}	microscopic	1.06	0.176	3.4×10^{-12}
EGDM	1.79	0.232	2.1×10^{-21}	EGDM	1.67	0.134	2.1×10^{-11}
ECDM	0.34	0.302	3.3×10^{-22}	ECDM	0.44	0.211	1.8×10^{-13}

TABLE 1.1 Lattice spacing, energetic disorder, and mobility at zero field and density extracted from a microscopic system and from fitting simulated hole mobilities to EGDM and ECDM for amorphous phases of (a) DCV4T and (b) DPBIC. DCV4T values: Reprinted with permission from J. Chem. Theory Comput., 2014, 10, pp 2508–2513. DPBIC values: Reproduced with permission from Adv. Funct. Mater., 2015, 25, pp 1955–1971.

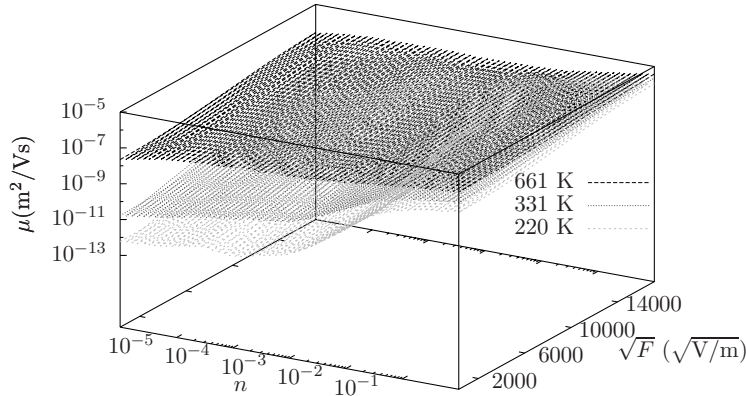


FIGURE 1.6 Hole mobilities for amorphous DPBIC as a function of the charge concentration n (number of charge carriers per site) after tabulation from simulations, smoothing and interpolation. Reprinted with permission from Phys. Chem. Chem. Phys., 2015, 17, pp 22778–22783 – Published by the PCCP Owner Societies.

to EGDM and ECDM teaches us that parameters of these models do not have a clear physical interpretation. Nevertheless, they still provide reasonable parametrizations and can eventually be used in conjunction with drift–diffusion equations, see Section 1.12.1. Figure 1.5 compares EGDM and ECDM fits to microscopic simulations for an amorphous mesophase of DCV4T.

On a technical side, the stochastic models described in Section 1.11.1 become very useful to perform the fits: They help to cover the required range of charge carrier densities and to reduce finite-size effects. Note, however, that finite size effects in systems with small charge carrier densities and large disorder are so large that the actual value of mobility is overestimated by several orders of magnitude [LA10]. In this case one needs to use the extrapolated mobility values [KSB⁺14].

1.11.3 Tabulated mobilities

Fitting the results of kinetic Monte Carlo simulations to the parametrizations provided by the EGDM or ECDM imposes a constraint on the functional form of $\mu(\rho, \vec{F}, T)$. To avoid this, one can tabulate the mobility in a wide range of charge densities, temperatures and electric fields. This tabulated function can then be used directly in the drift–diffusion equations solver [KSB⁺15]. The tabulation is computationally feasible only with the help of a stochastic model – otherwise it is not possible to reach the necessary system sizes and to span the wide density regime. Before using the tabulated function, it has to be interpolated and smoothed to ensure numeric stability [KSB⁺15]. Figure 1.6 shows the tabulated and smoothed mobility for amorphous DPBIC, which is eventually used to evaluate current–voltage characteristics of a DPBIC film, see Section 1.12.1.

1.12 Case studies

So far we have described various methodological developments and simulation approaches which can be used to simulate multilayered OLED structures. In the following sections we will show how these methods can be used to simulate steady-state current–voltage characteristics of an OLED, perform impedance spectroscopy simulations, estimate OLED efficiency, study electroluminescence of a white OLED, as well as to gain an insight into OLED stability.

1.12.1 Current–voltage characteristics

We will start by showing how the steady-state current–voltage characteristics of a single layer device can be simulated starting from the chemical structure of an organic semiconductor. As an example, we use a thin layer of DPBIC, a hole-conducting material, which is sandwiched between an ITO and aluminum electrode.

After parametrizing the DPBIC force field [KvdHAH⁺15], amorphous boxes of 4000 DPBIC molecules are simulated by MD simulations, as described in Section 1.10.2. The density of states of an amorphous solid state is then evaluated for holes using the perturbative scheme (see Section 1.7.2), yielding a mean value of 5.28 eV and an energetic disorder of $\sigma = 0.176$ eV. Density functional theory calculations (B3LYP/6-311g(d,p), see also Section 1.8) yield a hole reorganization energy of $\lambda = 0.068$ eV.

The reference system of 4000 molecules is further used to parametrize a stochastic algorithm (see Section 1.11.1) and to generate larger systems of 40000 sites (details can be found in Ref. [KSB⁺15]). Kinetic Monte Carlo simulations in large systems allow to tabulate charge mobility as a function of charge density, electric field, and temperature. The interpolated and smoothed tabulated function, depicted in Figure 1.6, is then used to solve the drift–diffusion equations, as described in Section 1.3. For the electrode ionization potentials we use average values of experimental reports: 4.73 eV for ITO [OHL⁺12, SMK01, WLL08, KBR⁺07] and 4.16 eV for Aluminum [Lid98]. These values, together with the DPBIC ionization potential, provide the value of the injection barrier which is required to solve the Poisson equation (1.3).

Without further microscopic calculations it is now possible to solve the drift–diffusion equations for film thicknesses of 203, 257 and 314 nm and temperatures of 233, 293 and 313 K, corresponding to different experiments. Figure 1.7 shows a comparison of simulated and experimental current–voltage curves in these situations. The agreement is remarkable for higher temperatures (293 K and 313 K). A possible reason for the larger differences at low temperatures are non-equilibrium processes, such as charge relaxation, which are not accounted for in our approach that relies on mobility parametrizations under stationary conditions. Another possibility is that the Marcus rate expression, equation (1.23), is no longer valid at these temperatures, since it is derived assuming a classical promoting mode and is valid only for high enough temperatures.

1.12.2 Impedance spectroscopy

In addition to studies of steady-state current–voltage characteristics, valuable insight into the functioning of organic devices can be obtained from impedance spectroscopy studies. In particular, impedance spectroscopy can provide information about carrier relaxation in the density of states (DOS), can help to distinguish between different trapping regimes in organic-semiconductor devices [KR11], and can be used to determine the width σ of the Gaussian DOS [MCCB14].

In impedance spectroscopy a dc bias V is applied over a device and, in addition to that, a small ac component $\Delta V(t) = \Delta V \exp(2\pi i f t)$ is added, where f is the frequency. The impedance $Z = Z' + iZ''$ is defined as the zero-amplitude limit of the ratio of $\Delta V(t)$ and the response

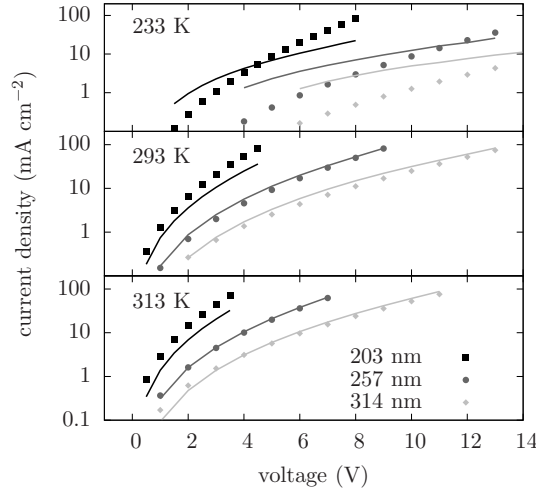


FIGURE 1.7 Current–voltage characteristics for DPBIC films of different thickness sandwiched between an ITO anode and an Aluminum cathode, measured at different temperatures. Theoretic predictions (lines) were obtained using parameter-free coupling of microscopic hole mobility data to drift–diffusion equations. Symbols are experimental results. Reprinted with permission from Phys. Chem. Chem. Phys., 2015, pp 22778–22783 – Published by the PCCP Owner Societies.

$\Delta I \exp [2\pi i(f + \phi)t]$ in the current, with ϕ a phase difference. Of particular interest is the capacitance–voltage, C – V , characteristic, with the capacitance given by $C = -Z''/2\pi f|Z|^2$.

Applying KMC simulations to extract the small response $\Delta I(t)$ is extremely cumbersome because of the noise present in such simulations. It has been shown, however, that for single-carrier organic devices the current–voltage characteristics obtained by solving the master equation are practically the same as those obtained from KMC simulations [vdHvOCB11]. The influence of small perturbations can be rather easily evaluated using the master equation. Within the framework of the time-dependent master equation the small ac component of the voltage in a single-carrier device leads to a time-dependent probability, $p_i(t)$, of the occupation of a site i by a charge, obeying Equation (1.14):

$$\frac{dp_i}{dt} = \sum_{j \neq i} [\omega_{ji}p_j(1 - p_i) - \omega_{ij}p_i(1 - p_j)] \equiv g_i(\vec{p}), \quad (1.34)$$

where \vec{p} is the vector of occupational probabilities of all sites.

Using a perturbative approach, first the steady-state solution, \vec{p}_0 , for $dp_i/dt = 0$ at the applied static voltage, V , has to be evaluated. The procedure for doing so has been described in Ref. [vdHUR⁺09]. Sheets of sites representing the electrodes are introduced at either side of a simulation box representing the device. An additional small-amplitude ac voltage with frequency f induces a small change, $\Delta \vec{p}$. Linearizing, we write $\vec{p}(t) \approx \vec{p}_0 + \exp(2\pi i f t) \Delta \vec{p}$ and $\vec{g}(\vec{p}) \approx \vec{g}(\vec{p}_0) + \exp(2\pi i f t) \left[\Delta V \partial \vec{g} / \partial V + \hat{J} \Delta \vec{p} \right]$, with the matrix elements of the Jacobian, \hat{J} , given by $J_{ij} = \partial g_i / \partial p_j |_{\vec{p}_0}$. Substituting these expressions into Equation (1.34) and linearizing leads to the equation

$$(2\pi i f \hat{I} + \hat{J}) \Delta \vec{p} = -\Delta V \frac{\partial \vec{g}}{\partial V}, \quad (1.35)$$

with \hat{I} denoting the identity matrix. Equation (1.35) can be solved for $\Delta \vec{p}$ with standard techniques, and from this the current, ΔI , and the capacitance, C , are readily obtained.

As an example, we consider two hole-only devices with the structure glass, indium tin oxide (100 nm), PEDOT:PSS (100 nm), LEP, Pd (100 nm). The light-emitting polymer (LEP) consists

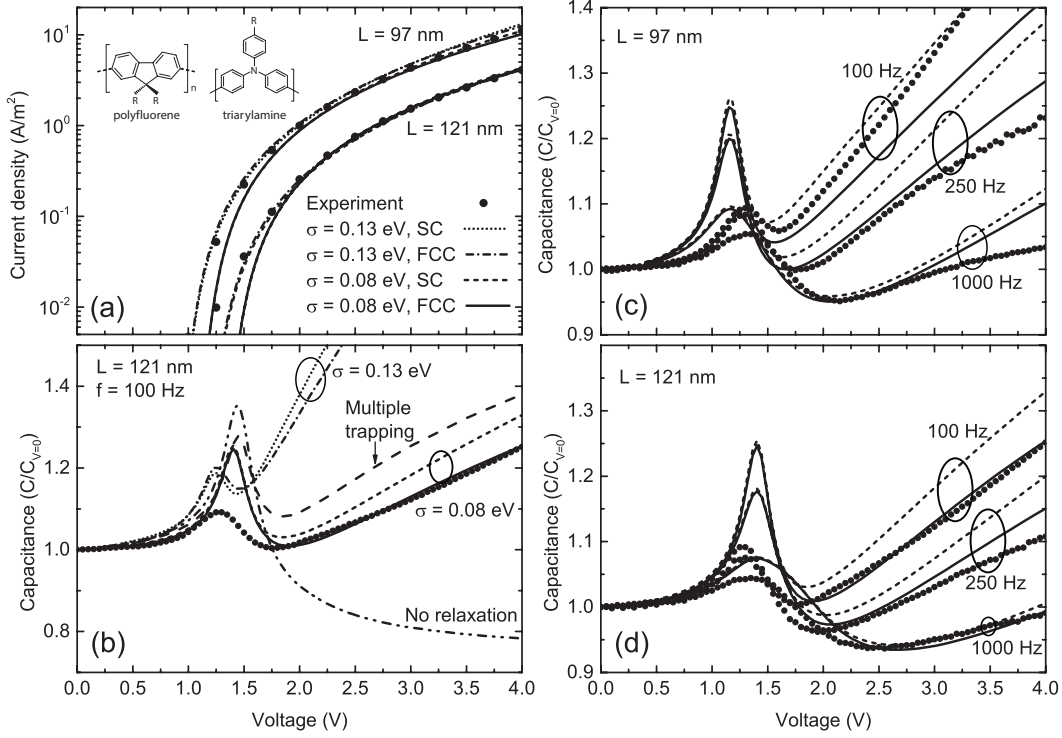


FIGURE 1.8 (a) Current density–voltage, J – V , characteristics of the devices with organic layer thicknesses $L = 97$ and $L = 121$ nm at $T = 295$ K. Dots: measurements [MSdG⁺13]. Curves: solutions of the steady-state master equation with $\sigma = 0.13$ and 0.08 eV for simple cubic (SC) and face-centered cubic (FCC) lattices. Inset: the used hole-transporting copolymer. (b) Capacitance, C , normalized to its value at $V = 0$, as a function of V at a frequency $f = 100$ Hz and temperature $T = 295$ K for the $L = 121$ nm device. Dots: measurements [GvdHvM⁺11]. Dash-dot-dotted curve: drift-diffusion calculation with an EGDM mobility function for $\sigma = 0.13$ eV, neglecting relaxation. Long-dashed curve: multiple-trapping result, which included relaxation [GvdHvM⁺11]. Other curves: solutions of the time-dependent master equation for $\sigma = 0.13$ and 0.08 eV and for SC and FCC lattices. (c) and (d) C – V characteristics at different frequencies for the $L = 97$ nm (c) and $L = 121$ nm (d) device. Dots: measurements [GvdHvM⁺11]. Curves: solutions of the time-dependent master equation. Reprinted from Appl. Phys. Lett. 104, 213301 (2014) with the permission of AIP Publishing.

of polyfluorene with 7.5 mol% copolymerized triarylamine units for hole transport; see the inset of Figure 1.8(a). The LEP-layer thicknesses are $L = 97$ and 121 nm for the two devices and their areas are $A = 9 \times 10^{-6}$ m². According to EGDM modeling studies of the current density–voltage, J – V , characteristics of these devices [vMVJC08, dVvMJC10] no injection barrier is present at the anode (PEDOT:PSS) and injection barriers of 1.65 and 1.90 eV are present at the cathode (Pd) for the $L = 97$ and $L = 121$ nm device, respectively. These modeling studies gave best fits for the J – V characteristics with $\sigma = 0.13$ eV.

We apply the above method to calculate the C – V characteristics of these two devices. Like in the EGDM studies [vMVJC08, dVvMJC10] we assume an uncorrelated Gaussian DOS with standard deviation σ . The use of Marcus rates Equation (1.6.1) would require knowledge of the reorganization energy λ_{ij} , which is not available here. We therefore assume Miller–Abrahams nearest-neighbor hopping with rates given by Equation (1.22). In absence of any morphological information we assume a regular lattice of hole-transporting sites. To investigate a possible influence of morphology we investigate simple cubic (SC) as well as face-centered cubic (FCC)

lattices with a lattice constant $a = 1.19$ nm for the SC lattice and $a = 1.88$ nm for the FCC lattice, in accordance with the known density $1.8 \times 10^{26} \text{ m}^{-3}$ of hole-transporting units. The simulation boxes have dimensions $L \times L_y \times L_z$, with $L_y = L_z = 50a$ and periodic boundary conditions in the y - and z - direction, yielding a sufficient lateral averaging. For further details we refer to Ref. [MCCB14].

As expected from the EGDM modeling [vMVJC08, dVvMJC10] it can be observed in Figure 1.8(a) that the experimental J - V characteristics (dots) at room temperature ($T = 295$ K) of the two devices are very well described by the solution of the steady-state master equation for $\sigma = 0.13$ eV, both for the SC (dotted curve) and the FCC (dash-dotted curve) lattice (a prefactor in the hopping rates was adjusted in both cases to obtain an optimal fit). However, this is not at all true for the C - V characteristics. It is seen in Figure 1.8(b) that for the $L = 121$ nm device solving the time-dependent master equation for $\sigma = 0.13$ eV at a frequency $f = 100$ Hz yields results that deviate strongly from the experimental C - V characteristic. The fact that the master-equation results for the SC and FCC lattice are quite comparable shows that this deviation is probably not due to a morphological issue.

In order to understand the problem better we first distinguish the different regimes in the C - V characteristics. (1) At low voltage all characteristics converge to the geometrical capacitance, because almost no carriers are present in the device. (2) With increasing voltage, a sheet of holes builds up by diffusion from the anode, but these cannot yet move to the cathode because the electric field is still directed from cathode to anode. As a result, the effective thickness of the device decreases and the capacitance rises. (3) When approaching the built-in voltage V_{bi} these holes start to move to the cathode, leading to a decrease of the capacitance. The result is a peak in the C - V curve before V_{bi} is reached [vMC08a]. (4) In the regime beyond V_{bi} the C - V curve rises again. Here relaxation effects play a dominant role and therefore this is the regime we want to focus on.

In order to identify the effects of relaxation we display in Figure 1.8(b) (dash-dot-dotted curve) the C - V characteristic obtained by solving the time-dependent drift-diffusion equation with the EGDM mobility function corresponding to $\sigma = 0.13$ eV. In this case the local mobility $\mu(x; \rho, F, T)$ depends on the instantaneous local charge density ρ and electric field F , and therefore contains no relaxation effects. It is seen that without relaxation effects the capacitance decreases after V_{bi} to a value that is even smaller than the geometrical capacitance. The long-dashed curve is the result of a multiple-trapping model for relaxation [GvdHvM⁺11]. With a fitted conduction-level energy $E_c = -0.75\sigma$ this model leads to a fair agreement with experiment.

Since solving the time-dependent master equation for $\sigma = 0.13$ eV apparently overestimates relaxation effects and since such effects decrease with decreasing σ we solved the time-dependent master equation for lower values of σ . With a value of $\sigma = 0.08$ eV we find a very satisfactory agreement with the experimental C - V characteristics, not only for the device and frequency considered in Figure 1.8(b), but for both devices and all considered frequencies; see Figs. 1.8(c) and (d). The only clear disagreement is in the peak, which is more pronounced in the calculations than in the experiment. This may be partially explained by lateral variations in V_{bi} of the devices [GvdHvM⁺11]. The dashed (SC) and full (FCC) curves in Figure 1.8(a) are the corresponding J - V curves obtained by solving the steady-state master equation. It is observed that for high voltages the experimental J - V curves are very well described, but significant deviations occur at low voltages around V_{bi} .

The analysis brings up the question why there is such an apparent discrepancy between the description of steady-state and time-dependent charge transport. A possible explanation is that in steady-state transport the low-energy tail of the DOS is important, represented by a relatively large σ , while in time-dependent transport relaxing carriers probe a larger part of the DOS, represented by a smaller σ . This would mean that the shape of the DOS is more complicated than a single Gaussian. It would also explain the difference in the description of the J - V curves in Figure 1.8(c). At low voltage, when carriers only occupy the low-energy tail

of the DOS, $\sigma = 0.13$ eV gives a better description, while at higher voltage, when the DOS is filled up further, $\sigma = 0.08$ eV provides an excellent description, which is even slightly better than with $\sigma = 0.13$ eV. A value of $\sigma = 0.13$ eV at low voltage could also partially explain the lower peak in the C - V curve as compared to the calculations with $\sigma = 0.08$ eV in Figs. 1.8(b)–(d). We note that the position of the peak could be improved by adapting the used built-in voltages V_{bi} . These voltages were obtained from an EGDM fit of the J - V characteristics with $\sigma = 0.13$ eV [vMVJC08, dVvMJC10], but should be optimized again in a fit with $\sigma = 0.08$ eV. In addition, EGDM neglects spatial correlations of site energies. This can lead to discrepancies when analyzing an experimental system with correlations in terms of a model without correlations [KA16].

The present conclusion that $\sigma = 0.08$ eV should be used to describe carrier relaxation in the considered devices is fully in agreement with the conclusion that dark-injection experiments on the same devices, which also probe carrier relaxation, can be described by solving a time-dependent master equation with the same value of σ [MSdG⁺13].

1.12.3 Efficiency

In OLEDs, electrical power is converted to a radiant flux (radiant energy emitted per unit time), Φ_e . The power efficiency, sometimes called the wall-plug efficiency, is given by

$$\eta_{\text{power}} = \frac{\Phi_e}{IV} = \frac{\int_0^\infty \Phi_{e,\lambda,\text{OLED}}(\lambda) d\lambda}{IV}, \quad (1.36)$$

with I the current, V the applied voltage, and $\Phi_{e,\lambda,\text{OLED}}$ the total optical power that is emitted externally per unit wavelength λ . The power efficiency is generally limited by inevitable Ohmic losses in the electrodes and in the organic charge transport layers, and sometimes also by Ohmic losses due to the presence of internal organic–organic energy barriers outside the emissive layer. When judging the efficiency of the conversion process in the emissive layer, one therefore often focuses on a complementary quantity, the external quantum efficiency η_{EQE} (EQE), which is defined as the total number of externally emitted photons per charge carrier which has passed the device

$$\eta_{\text{EQE}} = \frac{e}{I} \int_0^\infty \Phi_{e,\lambda,\text{OLED}}(\lambda) \frac{\lambda}{ch} d\lambda, \quad (1.37)$$

with e the fundamental charge, c the speed of light, and h the Planck constant. Due to full or partial internal reflection of light, not all photons which are internally generated will escape from the microcavity which is formed by the OLED layer structure. It is therefore useful to introduce an additional quantity, the internal quantum efficiency η_{IQE} (IQE), which is defined as the ratio of the total number of photons generated within the device and the number of electrons injected. The IQE is not directly measurable, but may be derived from the EQE using the expression

$$\eta_{\text{IQE}} = \frac{\eta_{\text{EQE}}}{\eta_{\text{out}}}, \quad (1.38)$$

with η_{out} the light-outcoupling efficiency. For emission from a specific position in a planar OLED microcavity, under a specific angle and for a specific wavelength, the (s and p) polarization dependent emitted light intensity may be obtained from optical simulations [Ney98, BKG⁺98, WHX⁺11, FMH⁺12]. The light-outcoupling efficiency is thus an effective value, which is determined by averaging over the entire emission profile and the entire emission spectrum and which is sensitive to the precise angular dependence of the emission from the dye molecules. Application of advanced emission profile reconstruction techniques [MCM⁺10, FMD11] and a measurement of the emitter orientation distribution [FYAB10] are required to determine η_{out} for a specific case with high precision. In the absence of such information, one often assumes that for well-designed phosphorescent OLEDs with a (glass | indium-tin-oxide (ITO) | organic semiconductor | Al) layer structure and with a random emitter orientation η_{out} is approximately

0.2. Larger values, up to $\sim 0.25 - 0.30$, are possible by optimizing all layer thicknesses [KK10]. Several methods, including the use of a roughened external glass surface or the use of internal high-refractive index scattering layers, have been developed to enhance the light-outcoupling efficiency to values above 0.5 [BFS⁺13, GR15].

Recently, much progress has been made in advanced molecular-scale kinetic Monte Carlo (KMC) calculations of the IQE [EBJC14, CvEBJ15, SG15]. We focus in this section on applications of KMC simulations to phosphorescent OLEDs based on a small concentration of metal-organic emitter molecules in a matrix material. In general, the IQE may be expressed as [BFS⁺13]

$$\eta_{\text{IQE}} = \eta_{\text{rec}}\eta_{\text{ST}}q_{\text{eff}}, \quad (1.39)$$

with η_{rec} the recombination efficiency, defined as the fraction of injected charges which contributes to exciton formation, η_{ST} the singlet–triplet factor, defined as the fraction of generated excitons which is quantum-mechanically allowed to decay radiatively, and q_{eff} the effective radiative decay efficiency, defined as the fraction of such excitons which actually decay radiatively. In phosphorescent OLEDs based on heavy metal-organic molecules, strong spin-orbit interaction gives rise to triplet states with some mixed-in singlet-character, so that also triplets are emissive and $\eta_{\text{ST}} = 1$. The recombination efficiency can be close to unity by making use of appropriate electron and hole blocking layers. A high effective radiative decay efficiency may be obtained, firstly, by using emissive dye materials with a large radiative decay rate, Γ_{rad} , and a small non-radiative decay rate, Γ_{nr} . In the absence of other loss processes, the IQE is then equal to $\Gamma_{\text{rad}}/(\Gamma_{\text{rad}} + \Gamma_{\text{nr}}) \equiv \eta_{\text{PL}}$, the photoluminescence (PL) efficiency. Non-radiative decay is a result of the nuclear motion, so that the energy of the molecule in its excitonically excited state can be equienergetic with a highly vibrationally excited excitonic ground state [Lan12]. Secondly, the matrix material and the adjacent blocking material should have a triplet energy level significantly larger than the dye triplet level, so that the triplet excitons stay confined to the dye sites. These design rules are already relevant to the IQE at small current densities. Experimentally, the IQE is found to depend on the current density, J . At large J , η_{IQE} decreases with increasing J . For some devices, η_{IQE} is found to show a broad maximum before the decrease (“roll-off”) sets in. A practical measure is the current density J_{90} at which the IQE has decreased to 90% of the maximum value. For efficient phosphorescent OLEDs, maximum reported values of J_{90} are approximately 300 A/m^2 [MLG13]. In commercial white OLEDs for lighting conditions, operated at high luminance levels, the efficiency loss due to roll-off can be indeed of the order of 10 percent.

Understanding the roll-off is not only important as a first step towards enhancing the efficiency. Loss processes which limit the IQE at high J can also trigger local degradation processes with a certain probability, as it will be discussed in Section 1.12.5. By building “virtual OLEDs” in which the interplay of all charge transport and excitonic processes is included mechanistically using KMC simulations, the functioning of OLEDs can be studied with sub-nanosecond time and molecular-scale spatial resolution. The first demonstration of the feasibility of such an approach was presented by van Eersel *et al.* [EBJC14]. We discuss their simulation results for OLEDs based on the green-emitting metal-organic molecule tris[2-phenylpyridine]iridium ($\text{Ir}(\text{ppy})_3$) and the red phosphorescent dye platinum octaethylporphyrin (PtOEP).

The simulations were based on the three-dimensional (3D) kinetic Monte Carlo code: For a detailed discussion of the model used, we refer to Refs. [EBJC14, CvEBJ15, MCdV⁺13, EBC15]. Ref. [EBJC14] also gives motivations for the parameter values used, and provides analyses of the sensitivity of the simulation results to the parameter values. Briefly, the OLEDs were modeled as a collection of molecular sites on a simple cubic lattice. For each type of molecule, the site energies for electrons and holes were taken randomly from a Gaussian density of states (DOS) with an average energy as given in Figure 1.9(a). Charges were assumed to hop with a rate as described within the Miller–Abrahams formalism, Equation (1.22). The hopping attempt fre-

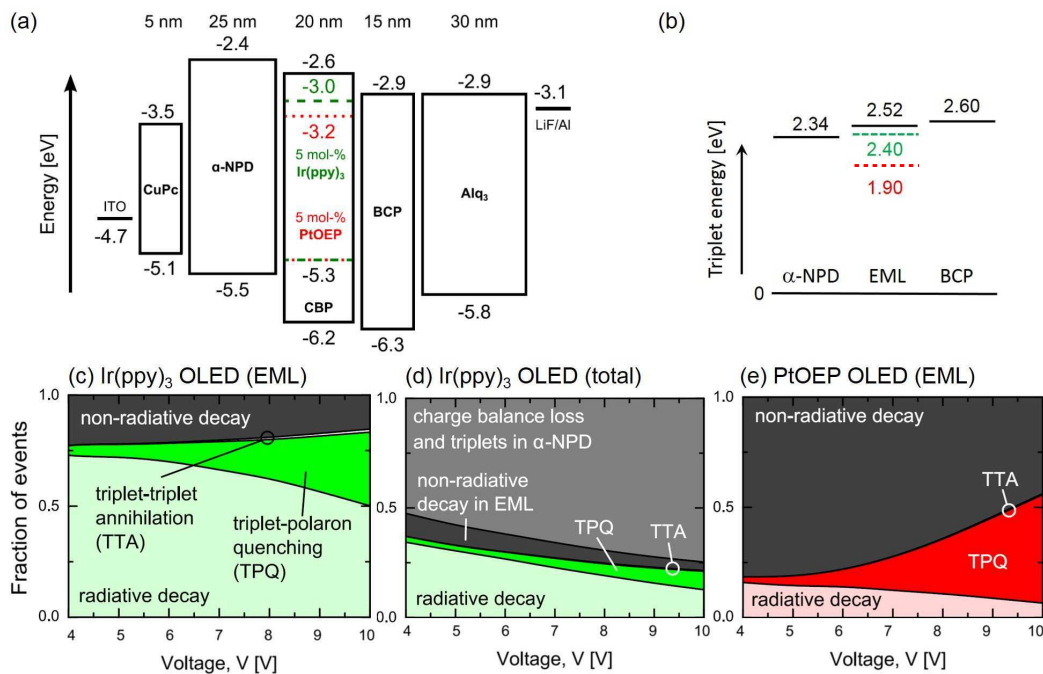


FIGURE 1.9 (a) Energy level and layer structure of the green and red OLEDs studied in Ref. [EBCJ14]. The phosphorescent emissive layer (EML) is sandwiched in between materials facilitating hole and electron injection, transport and blocking: CuPc (copper phthalocyanine), α -NPD (4,4'-bis[N-(1-naphthyl)-N-phenyl-amino] biphenyl), BCP (2,9-dimethyl, 4,7-diphenyl, 1,10-phenanthroline) and Alq₃ (tris [8-hydroxyquinoline] aluminum). (b) Triplet energies for the materials used in the EML (solid line: CBP; dashed line: Ir(ppy)₃; dotted line: PtOEP) and the layers adjacent to the EML. (c)–(e) Contribution of the various exciton decay processes in the EML of the Ir(ppy)₃ device (b), in the entire Ir(ppy)₃ device (c), and in the EML of the PtOEP device (d). The figures show that even above 6 V only a small fraction of the efficiency loss (less than 2% (0.5%) for the Ir(ppy)₃ (PtOEP) devices) is due to TTA. Reprinted from Appl. Phys. Lett. 105, 143303 (2014) with the permission of AIP Publishing.

Parameter	Description	Value	
<i>Common</i>			
ω_0	hopping attempt frequency to the first neighbor	$3.3 \times 10^{10} \text{ s}^{-1}$	
σ	width of the electron and hole Gaussian DOS	0.10 eV	
N_t	site density	$1.0 \times 10^{27} \text{ m}^{-3}$	
$\lambda \equiv 1/\gamma$	wavefunction decay length	0.3 nm	
ϵ_r	relative dielectric permittivity	3.5	
σ_T	width of the triplet exciton DOS	0.10 eV	
$E_{T,b}$	triplet exciton binding energy	1.0 eV	
k_D	prefactor for triplet exciton Dexter transfer	$1.6 \times 10^{10} \text{ s}^{-1}$	
<i>Material-specific</i>			
R_F	Förster radius for triplet exciton diffusion	Ir(ppy) ₃	PtOEP
		1.5 nm	1.5 nm
Γ_{rad}	radiative decay rate	$0.816 \mu\text{s}^{-1}$	$0.1 \mu\text{s}^{-1}$
Γ_{nr}	non-radiative decay rate	$0.249 \mu\text{s}^{-1}$	$0.525 \mu\text{s}^{-1}$

TABLE 1.2 Overview of the simulation parameters. The HOMO and LUMO energies are given in Figure 1.9(a), and the triplet energies are given in Figure 1.9(b).

quency ω_0 and the wavefunction decay length $\lambda = 1/\gamma$ were taken equal for all pairs of sites. The simulations included the Coulomb interactions between all charge carrier pairs, and with image charges in the metallic electrodes. In a natural way, the formation of space-charge layers near the injecting and organic–organic interfaces, and the resulting “band bending” was thus included. Cottaar *et al.* have demonstrated that in energetically disordered materials, as they are used in OLEDs, explicitly taking the individual 3D Coulomb interactions into account is important for properly treating charge accumulation near internal interfaces [CCB12]. Instantaneous intersystem crossing was assumed, so that only triplet excitons were considered. Exciton generation and dissociation were treated in the same way as hops of electrons and holes, but including the triplet exciton binding energy. Radiative and non-radiative triplet exciton decay was included, as well as exciton transfer between the dye molecules, leading to exciton diffusion. The transfer rate was expressed as a sum of Förster-type and Dexter-type contributions, Equations 1.25 and 1.26, with $\tau = (\Gamma_{\text{rad}} + \Gamma_{\text{nr}})^{-1}$ the effective decay time, R_F the Förster radius for diffusion and k_D the Dexter prefactor. The two bimolecular loss processes which potentially contribute to the IQE roll-off, triplet–polaron quenching (TPQ) and triplet–triplet annihilation (TTA), were both included in a parameter-free manner, viz. by assuming an infinite (zero) rate when an exciton and a polaron or two excitons, respectively, are present on nearest neighbor (more distant) sites. Table 1.2 gives an overview of the used parameter values.

Figures 1.10(a) and (b) show a comparison of the calculated and experimental J – V and IQE roll-off curves, respectively, for a temperature 300 K. The slope of the J – V curves is well-described, but the absolute value of the current density is somewhat overestimated. As argued in Ref. [EBJC14], this might be related to an underestimation of the HOMO-LUMO gap, which was taken to be equal to the optical gap. This often-used approach neglects the exciton binding energy, which can be around 1 eV [YY15]. Such a correction would horizontally shift the J – V curves by 1 eV, giving rise to significant reduction of the discrepancy. The roll-off curve would not be affected by such a correction. We note that (as mentioned above) the triplet exciton binding energy was included when calculating the rates of exciton generation and dissociation processes. For Ir(ppy)₃, the simulation results agree within the error margin with experiment, whereas for PtOEP the roll-off is slightly underestimated at high current densities. A sensitivity analysis was carried out to find out which uncertainties in the choice of parameter values have the largest impact. It was found, e.g., that the J – V characteristics are quite strongly determined by the energy level differences at interfaces and between the host and guest states in the EML. The sensitivity to the hopping attempt frequency was found to be relatively small.

The simulations provided detailed views on the cause of the roll-off, as shown in Figures 1.9(c)–(e). In both devices, most of the emission was found to occur near the anode-side of the EML. This may be understood from Figure 1.9(a), from which the guest molecules are expected to give rise to stronger hole trapping than electron trapping. As a result, the effective

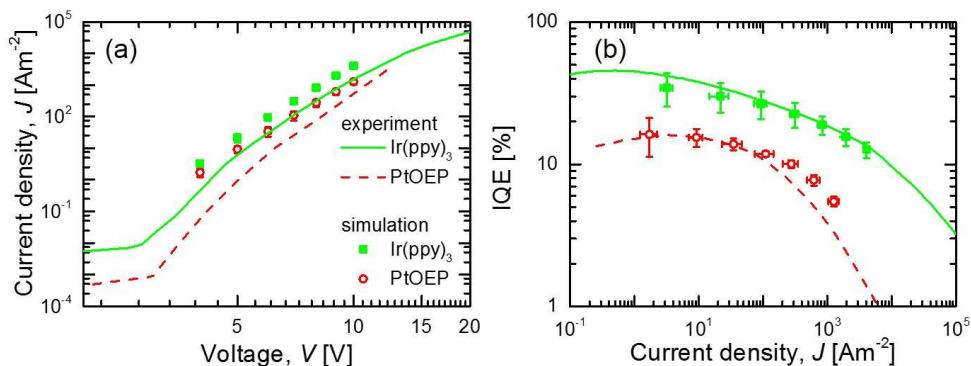


FIGURE 1.10 (a) Simulated and experimental J - V characteristics. (b) Simulated IQE and experimental IQE (assuming 20% outcoupling efficiency) as a function of the current-density. Experimental data from Ref. [GF08]. Reprinted from Appl. Phys. Lett. 105, 143303 (2014) with the permission of AIP Publishing.

electron mobility is larger than the hole mobility. In the emissive layer, most of the IQE loss was found to be due to TPQ, and only at high voltages a small TTA contribution was found (Figure 1.9(c)). For the $\text{Ir}(\text{ppy})_3$ devices, the overall loss was found to be determined mostly by a non-ideal recombination efficiency due to imperfect electron blocking and by triplet exciton diffusion to the α -NPD layer (Figure 1.9(d)). The finding of electron loss to the α -NPD layer is consistent with the observation of some blue emission from that layer [GF08]. Due to subsequent TPQ, triplet transfer to the α -NPD layer gives also rise to a loss. From simulations, improving the devices by introducing perfect electron blocking was predicted to give rise to a 10% increase of the IQE at small voltages, from $\sim 34\%$ to $\sim 44\%$. The IQE at small voltages was found to become equal to the PL efficiency assumed (77%) when also the triplet transfer to the hole transport layer was eliminated. For the red devices, at low voltages no significant electron and triplet loss to the α -NPD layer was found, as may be understood from the lower LUMO energy and the smaller triplet energy of PtOEP. The IQE is then close to the PL efficiency assumed (16.4%).

1.12.4 Electroluminescence of a white OLED

The KMC simulations described in Section 1.5 can be employed to model all molecular-scale electronic processes that finally lead to electroluminescence of an OLED: injection, transport, and recombination of electrons and holes as well as diffusion and radiative decay of excitons. We will consider here the white multilayer OLED stack of Figure 1.11(a), which was studied experimentally and by KMC simulations in Ref. [MCdV⁺13]. It concerns a so-called “hybrid” OLED, which combines red and green phosphorescent emission with blue fluorescent emission. Phosphorescent emission can be very efficient because of the harvesting of both singlet and triplet excitons, see Section 1.2.4. However, since stable blue phosphorescent emitters with long-term stability are to date unavailable, many commercial white OLEDs make use of blue fluorescent emission, despite the fact that then only singlet excitons are harvested.

The working principle of the OLED of Figure 1.11(a) is the following. Holes reach the light-emitting layers of the stack after being injected by an ITO layer into a 4 mol% p -doped injection layer of NHT5:NDP2 and transported through a hole-transporting and electron-blocking layer of α -NPD (N,N' -di(naphthalen-1-yl)- N,N' -diphenyl-benzidine). Electrons reach the emitting layers after being injected by an aluminium cathode into a 4 mol% n -doped electron-injection layer and transported through an electron-transporting and hole-blocking layer of NET5. Blue light is generated in a 10 nm thick fluorescent layer of Spiro-DPVBi (2,2',7,7'-tetrakis(2,2-

Material	E_{HOMO} (eV)	E_{LUMO} (eV)	$\mu_{0,\text{h}}$ (m^2/Vs)	$\mu_{0,\text{e}}$ (m^2/Vs)	c_{trap}	T_0 (K)
NHT5:NDP2	-5.10					
α -NPD	-5.43	-2.33	6×10^{-9}	6×10^{-10}		
Ir(MDQ) ₂ (acac)	-5.13	-2.93	6×10^{-9}	6×10^{-10}		
TCTA	-5.60	-2.20	2×10^{-8}	2×10^{-9}		
Ir(ppy) ₃	-5.20	-2.70	2×10^{-8}	2×10^{-9}		
TCTA	-5.60	-2.20	2×10^{-8}	2×10^{-9}		
TPBi	-6.20	-2.60	2×10^{-8}	2×10^{-9}		
Spiro-DPVBi	-5.70	-2.80	6×10^{-9}	8×10^{-9}	0.001	2350
NET5	-6.00	-2.50	1.5×10^{-11}	1.5×10^{-10}	0.005	1400
NET5:NDN1		-2.50				

TABLE 1.3 HOMO and LUMO energies, room-temperature hole- and electron-mobilities $\mu_{0,\text{h}}$ and $\mu_{0,\text{e}}$ at low field and low carrier density, electron-trap concentration c_{trap} , and trap temperature T_0 of the exponential trap DOS in the different layers of the stack, as used in the KMC simulations [MCdV⁺13].

diphenylvinyl)Spiro-9,9'-bi fluorene) adjacent to the NET5 layer. Green light is generated in a 3 nm thick layer of TCTA (4,4',4''-tris(N-carbazoyl)-triphenylamine) doped with 8 mol% of the green phosphorescent dye Ir(ppy)₃ (fac-tris(2-phenylpyridyl)iridium). Red light is generated in a 20 nm thick α -NPD layer doped with 5 mol% of the red phosphorescent dye Ir(MDQ)₂(acac) ((acetylacetonate)bis(2-methyldibenzo[f,h]quinoxinalate)iridium).

The green phosphorescent layer is separated from the blue fluorescent layer by a thin (3 nm) interlayer consisting of a mixture of the hole-transporter TCTA with 33 mol% of the electron-transporter TPBi (1,3,5-tris(N-phenylbenzimidazol-2-yl)benzene). This interlayer has several purposes [SRR⁺09]. It should block the transfer of singlet excitons from the blue to the green layer and of triplet excitons from the green to the blue layer (Spiro-DPVBi has a triplet energy lower than that of Ir(ppy)₃). Also, this interlayer should allow the passage of electrons from the blue to the green layer (by the TPBi) and of holes from the green to the blue layer (by the TCTA). The red phosphorescent layer is on purpose in direct contact with the green phosphorescent layer, allowing triplet excitons formed on the phosphorescent dye in the green layer to diffuse to the phosphorescent dye in the red layer. This diffusion is an important process in establishing the right color balance.

The measured room-temperature current density–voltage characteristic of the OLED is shown in Figure 1.11(b). The arrow indicates the bias voltage of 3.6 V for most of the reported results. The CIE 1931 color point of the perpendicularly emitted light at this bias was measured to be $[x, y] = [0.47, 0.45]$, which corresponds to warm-white emission. The external quantum efficiency (EQE), i.e., the fraction of emitted photons per injected electron-hole pair, is measured to be $5 \pm 1\%$ [MCdV⁺13]. Figure 1.11(c) shows the color-resolved emission profile, which was reconstructed with a precision on the order of a nanometer from the measured angle- and polarization-dependent emission spectra [MCdV⁺13, MCM⁺10]. It is observed that in the blue layer, the emission occurs close to the interface with the interlayer and in the red layer close to the interface with the green layer.

The KMC simulations of the charge dynamics were carried out in the following way. Point sites arranged on a cubic lattice with a lattice constant $a = 1$ nm, the typical intermolecular distance of the used molecular semiconductors, represent the molecules in the stack. A simulation box of $50 \times 50 \times 56$ sites with periodic boundary conditions in the lateral (x and y) directions was used, which turned out to yield sufficiently accurate results. Since charge transport in various small-molecule materials was found to be described well by the ECDM [vMVJC08, vMdVS⁺10], correlated disorder caused by random dipoles was assumed for the electron and hole energies. The energetic disorder was taken to be $\sigma = 0.1$ eV, corresponding to the value found for hole transport in α -NPD [vMVJC08]. With this value the charge transport in all materials in the stack is expected to be reasonably described. Red and green emitting guests were introduced according

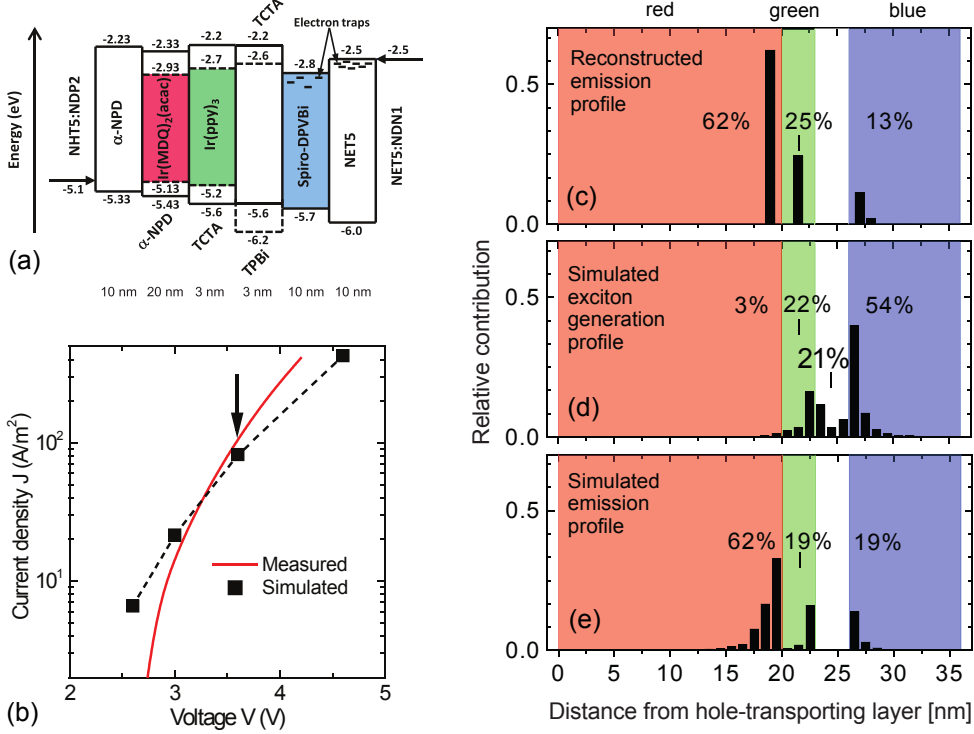


FIGURE 1.11 (a) Stack structure of the investigated white OLED with the different layers and their thicknesses. The HOMO and LUMO energy levels as used in the KMC simulations are indicated by solid lines for host materials and dashed lines for guest materials. The horizontal arrows indicate the work functions used for the doped hole- and electron-injecting layers. Electron traps were assumed in the Spiro-DPVBi and NET5 layers with concentrations of 10^{-3} and 5×10^{-3} , and characteristic energies $k_B T_0 = 0.2$ and 0.12 eV, respectively, of their exponential DOS. (b) Measured and simulated room-temperature current density-voltage, J - V characteristics. All other presented results are for the bias voltage $V = 3.6$ V, indicated by the arrow. The relative error in the simulated current density is estimated to be about 10%. (c) Emission profile reconstructed from the measured angle- and polarization-dependent emission spectrum [MCdV⁺13]. The percentages of red, green, and blue emission are indicated. (d) Exciton generation profile as obtained from the KMC simulations. (e) Emission profile as obtained from the KMC simulations, after taking into account exciton diffusion and the radiative decay probabilities of the emitters. The error in the simulated profiles is about 1%. Reprinted by permission from Macmillan Publishers Ltd: Nature Materials 12, p. 652 (2013).

Material	$\Gamma_{\text{rad}} (\mu\text{s}^{-1})$	$\Gamma_{\text{nr}} (\mu\text{s}^{-1})$	R_F (nm)	E_T (eV)
Ir(MDQ) ₂ (acac)	0.588	0.112	1.5	2.0
Ir(ppy) ₃	0.816	0.249	1.5	2.4

TABLE 1.4 Radiative and non-radiative exciton decay rates Γ_{rad} and Γ_{nr} , Förster radii R_F for exciton transfer between phosphorescent emitter molecules, and triplet energies E_T . For the green emitter Ir(ppy)₃ Γ_{rad} and Γ_{nr} were taken from Ref. [MRN09]. For the red emitter Ir(MDQ)₂(acac) $k\Gamma_{\text{rad}}$ was obtained from Ref. [TLC04], and Γ_{nr} from η_r given in Ref. [FMH⁺12] and the relation $\eta_r = \Gamma_{\text{rad}}/(\Gamma_{\text{rad}} + \Gamma_{\text{nr}})$. The value $R_F = 1.5$ nm for transfer between equal emitter molecules is a typical value given in Ref. [KBB⁺06]. According to the estimate in Ref. [SKHW12] we took $R_{F,\text{GR}} = 3.5$ nm for the transfer from a green to a red emitter. The triplet energies were taken from Ref. [SRR⁺09].

to the known concentration of the emitters, with appropriately adapted energy levels. Electron traps were introduced in the layers in which electron transport is important: the blue fluorescent layer and the electron-transporting layer. They were modeled with an exponential DOS of trap energies [MdBPB07, MBLA12, OMM⁺12] with a concentration c_{trap} and a characteristic energy $k_{\text{B}}T_0$.

Nearest-neighbor hopping of charges on the lattice using the Miller–Abrahams rate Equation (1.22) was assumed. The energy differences in the hopping rates contain, apart from the random site energies, an electrostatic contribution due to the bias applied to the OLED and the Coulomb energy due to all present charges. The doped injection layers were treated as metallic, injecting and collecting charges with an energy according to their work function, indicated by the arrows in Figure 1.11(a). Exciton generation was assumed to occur by hopping of an electron to a site where a hole resides, or vice versa, and was assumed to be always an energetically downward process.

Table 1.3 gives the parameters of the stack materials used in the KMC simulations of the charge dynamics. The parameters were determined from charge-transport and spectroscopic studies of the various materials [MCdV⁺13]. Exciton diffusion within the green and red layers and from the green to the red layer was included in the simulations. Since the red and green emitters trap electrons as well as holes (see the energy level scheme in Figure 1.11(a)), almost all excitons in the red and green layer are generated on the emitters. The diffusion of excitons among the emitters was described by Förster transfer, Equation 1.25, made possible by the spin-singlet character that is mixed into the exciton wave function by the spin-orbit coupling of the heavy iridium atoms. Apart from being transferred, excitons can decay radiatively with a rate $\Gamma_{\text{rad},i} = 1/\tau_{\text{r},i}$, or non-radiatively with a rate $\Gamma_{\text{nr},i} = 1/\tau_{\text{nr},i}$. These rates are related to the radiative decay probabilities η_r by $\eta_{r,i} = \Gamma_{\text{rad},i}/(\Gamma_{\text{rad},i} + \Gamma_{\text{nr},i})$. We took $\eta_r = 0.84$ and 0.76 for the red and green phosphorescent emitter in their respective hosts [FMH⁺12]. Other parameters used in the exciton dynamics are given in Table 1.4. Only exciton transfer from green to red was taken into account. Transfer from red to green should be negligible.

For each exciton generated in the red or green layer a separate simulation of its dye-to-dye diffusion and final radiative or non-radiative decay was performed. This diffusion was assumed to proceed independently from all other processes, which means that exciton quenching processes were neglected. Excitons generated on host sites in the red and green layer (a small fraction) were assumed to transfer instantaneously to an emitter in their neighborhood. Diffusion of excitons generated in the blue layer was not accounted for, because the diffusion length of these excitons is short and because their transfer to the green layer is blocked by the interlayer. We assumed that in the blue fluorescent layer singlet and triplet excitons are generated in a quantum-statistical ratio of 1:3 and that the triplet excitons are lost. For the radiative decay probability of singlet excitons in the blue layer we took $\eta_r = 0.35$ [LKZ⁺06]. Excitons generated in the interlayer were assumed to be lost by non-radiative decay or emission outside the visible spectrum.

The J – V characteristic following from the KMC simulations is given in Figure 1.11(b). Considering the various simplifications that were made, the agreement with the measured characteristic is fair. The underestimation of J at high voltage could be due to a heating effect, while the overestimation of J at low voltage could result from a systematic underestimation of the LUMO energies due to neglect of the exciton binding energies. At the bias voltage of 3.6 V for most of the reported results, the experimental and simulated current density agree quite well.

Figs. 1.11(d) and (e) present the simulated exciton generation profile and emission profile, respectively, at 3.6 V. The effect of exciton transfer from green to red is clearly observable and is very important for the color balance of this OLED. The simulated emission profile is in fair agreement with the reconstructed emission profile from Figure 1.11(c). The broadening of the simulated emission profile over a few nanometers in the red layer found in the simulations is not seen in the reconstructed emission profile, but this could be due to the limited resolution of the reconstruction procedure [MCdV⁺13, MCM⁺10]. The total percentages of emission in the red,

green, and blue agree quite well with the reconstructed emission profile.

The results presented in this section show that KMC simulations of all molecular-scale electronic processes leading to electroluminescence in quite complicated multilayer OLEDs with commercial relevance are feasible. The parameters in the present study were almost all obtained from experimental studies, but there is no obstacle for obtaining these from first-principles computational studies. Complete *in silico* studies of the functioning of commercial OLEDs therefore seem to be within reach.

1.12.5 Degradation

Developing an improved understanding of the mechanisms which limit the operational lifetime of OLEDs is of key importance towards the further adoption of OLED technology for display, lighting and signage applications. Experimentally, given fixed current density and ambient temperature conditions, the luminance is often observed to decrease with time in an approximately exponential or stretched-exponential manner. For commercial white OLEDs for lighting applications, the time at which the luminance has dropped to 70% of the initial value (the so-called LT_{70} lifetime) can today be as large as 10,000 hours or more at a luminance of 8,000 cd/m². However, long lifetimes are in practice often realized by making a trade-off with device efficiency (e.g. when using hybrid OLEDs, see Section 1.12.4) or production cost and ease of manufacturing (e.g. when using multiply vertically stacked OLEDs). Examples of other aspects of OLED reliability during prolonged operation are the voltage stability (at a fixed current density), the color point stability, the stability at high ambient temperatures and the stability under prolonged exposure to the ambient atmosphere [AP04, SK10]. The latter issue, leading to so-called black-spot formation, has been mitigated by the development of improved encapsulation technologies [PCCL11]. Recently, an excellent overview of the degradation mechanisms and reactions in OLEDs has been given by Scholz *et al.* [SKLL15].

In this section we focus on the use of molecular-scale OLED device modeling as a means to elucidate the role of various possible intrinsic degradation processes, i.e., processes which are caused by excitons (including those due to absorption of internally emitted photons), charges, and fields in the opto-electronically active organic semiconducting layer. When setting up an extension of the KMC simulations described in Sections 1.5 and 1.12.3, in order to include degradation, first an inventory should be made of the processes which for a specific system are expected to give rise to degradation. Formally, a distinction should be made between: (i) monomolecular degradation processes, which occur when the state of a single specific molecule is modified, e. g. due to the presence of a polaron or an exciton or due to a local electric field, and (ii) bimolecular degradation processes, which occur upon an interaction between charges and/or excitons on two different molecules, e. g. exciton–exciton annihilation or exciton–polaron quenching.

Including these two types of degradation processes requires a rate and a probability, respectively, as well as a description of the resulting changes of the KMC parameter values. Monomolecular degradation has been observed, e.g., in OLEDs containing the electron transport material tris(8-hydroxyquinoline)aluminum (Alq₃), in which the presence of holes gives rise to a reduction of the emission by the formation of fluorescence quenchers [APH⁺99]. Degradation due to the presence of singlet excitons has been reported for 4,4'-bis(N-carbazolyl)biphenyl (CBP), used as a matrix material in the EML of green-emitting phosphorescent OLEDs [KLN07]. The degradation products can act as nonradiative recombination centers and trap states. Degradation due to singlet excitons has also been reported for OLEDs based on the fluorescent emitter material 2,2',7,7'-tetrakis(2,2-diphenylvinyl)spiro-9,9'-bifluorene (spiro-DPVBi) [SSLL10]. An example of a bimolecular process which can be accompanied by degradation is triplet–polaron quenching (TPQ). When TPQ is due to excitation of the polaron by the triplet exciton, followed by non-radiative decay of the excited polaron due to internal conversion, the locally dissipated energy

may, with a certain probability, lead to a chemical change of the molecule. Such a mechanism was found for a blue phosphorescent OLED using 4,4'-bis(3-methylcarbazol-9-yl)-2,2'-biphenyl (mCBP) as the host material in the EML [GDW⁺08]. The mCBP defect sites were argued to act as deep charge traps, and the dissociation products were argued to damage the guest (emitter) so that it becomes a non-radiative center and a luminescence quencher.

A KMC degradation study starts in general with running a simulation without degradation until dynamic equilibrium is achieved under the operational conditions (voltage, temperature) of interest. Subsequently, the simulations are continued while degradation is switched on. Monomolecular degradation due to a charge or an exciton on a sensitive site is included as a new possible process which competes with all other possible processes. Degradation which accompanies a bimolecular process such as TPQ is included by branching the end result of that process, so that with a certain probability a defect site is formed. We note that in KMC simulations only the primary event needs to be described. All subsequent effects (e.g. a shift of the recombination zone to a less favorable position due to a changed mobility balance, or an efficiency loss due to TPQ at charges residing on defect molecules which act as traps [SJN⁺15]) will follow “automatically” from the simulations. KMC lifetime simulations are necessarily strongly accelerated, as practically realistic simulated times are usually at most of the order of 1 ms, six to eleven orders of magnitude smaller than actual lifetimes in the range of 1 to 100,000 hours. This can be accomplished by assuming an enhanced value of the degradation rate (for monomolecular degradation) or the degradation probability (for degradation accompanying a bimolecular process). As in the case of experimental OLED lifetime tests, it is also possible to accelerate the simulations by carrying them out for high current densities and/or elevated temperatures, followed by extrapolation to application-relevant operational conditions.

A first demonstration of the feasibility of three-dimensional kinetic Monte Carlo OLED lifetime simulations was presented in Ref. [CvEBJ15]. The simulations were carried out for a symmetric OLED with an energy level structure as shown in Figure 1.12(a), for a temperature 300 K. The mixed-matrix emissive layer contains equal concentrations of the hole transport layer (HTL) and electron transport layer (ETL) material as a host, and 4 mol% of emitter molecules (guest). The hole and electron blocking is excellent, so that the recombination efficiency is 100%. The simulation parameters are as given in Table 1.2, with the following exceptions: $\varepsilon_r = 3$, $\sigma_T = 0$ eV (no triplet energy disorder), $\Gamma_{\text{rad}} = 0.544 \mu\text{s}^{-1}$ and $\Gamma_{\text{nr}} = 0.181 \mu\text{s}^{-1}$ (values typical for the orange-red emitter Ir(MDQ)₂(acac) in an α -NPD matrix [SSF⁺11]). As in Section 1.12.3, TPQ and TTA were treated in a parameter-free manner as instantaneous nearest-neighbor processes.

Van Eersel *et al.* [EBJC14] showed that for these symmetric devices and with a dye trap depth $\Delta = 0.2 - 0.3$ eV the emission profile at small voltages is quite uniform across the emissive layer. This is illustrated by Figure 1.12(b), which shows the emission profile at 3 V for the case studied ($\Delta = 0.2$ eV). On the one hand, this choice avoids a large Ohmic loss due to deep trapping and a large overvoltage due to the enhanced built-in voltage (for large Δ). On the other hand, it also avoids a large loss due to strong roll-off caused by emission from thin zones near the blocking layer interfaces (for small Δ). The optimum value of Δ will depend on the application goal (see Ref. [EBJC14]) and is sensitive to the detailed mechanisms of the TPQ and TTA processes. Figure 1.12(c) shows the calculated IQE roll-off curve before degradation. The J - V curve is given in the inset. At small voltages, the IQE is equal to the assumed radiative decay (PL) efficiency ($\eta_{\text{rad}} = \Gamma_{\text{rad}}/(\Gamma_{\text{rad}} + \Gamma_{\text{nr}}) = 0.75$). The J_{90} current density, defined in Section 1.12.3, is approximately 640 A/m². This is larger than the largest experimental value obtained so far (~ 300 A/m², see Section 1.12.3). The full curve gives a fit through the data points, discussed below (Equation (1.41)). For the nearest-neighbor TPQ and TTA mechanisms considered, the roll-off is almost completely due to TPQ.

Figure 1.12(d) shows the dependence of the normalized emission on the simulated time, at constant voltage conditions (6 V), for a degradation scenario in which, upon a TPQ process, the

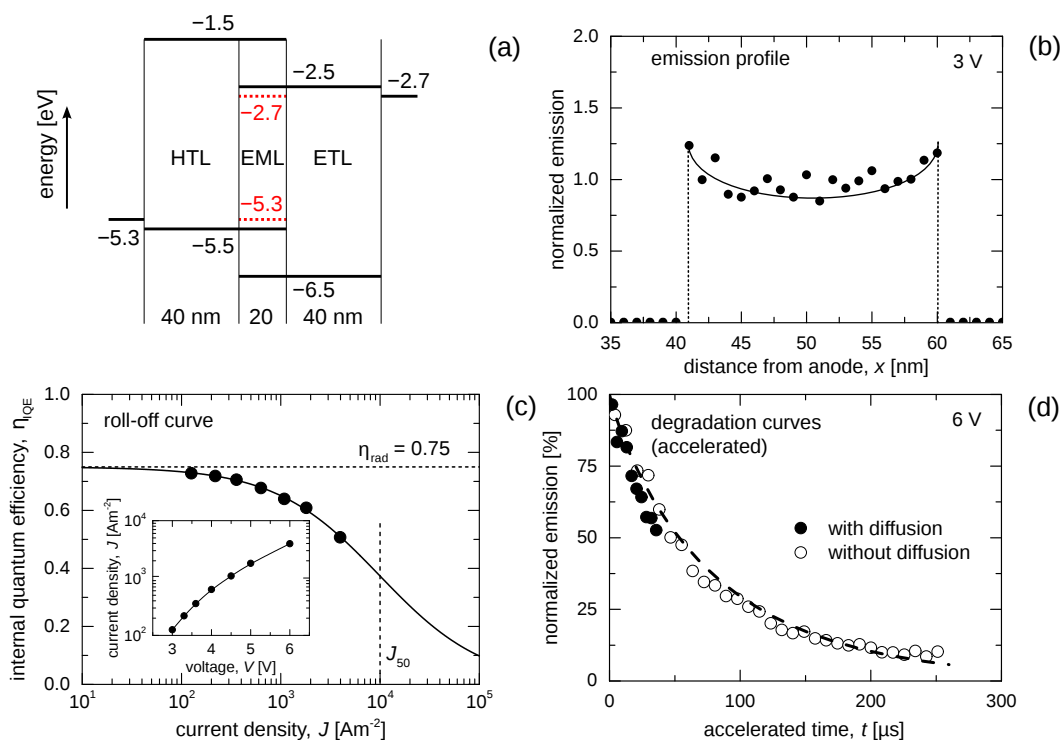


FIGURE 1.12 (a) Organic layer and energy level structure of the OLEDs considered in the KMC degradation simulation studies. Red dashed lines: emitter energy levels (4 mol%). (b) Emission profile at 3 V. The full curve is a guide-to-the-eye. (c) Current density dependence of the internal quantum efficiency. The full curve is a fit using Equation (1.41) with $m = 0.80$ and $J_{50} = 10 \text{ kA/m}^2$. The vertical dashed line indicates the current density at which the IQE has dropped to 50% (J_{50}) of the value at small current densities. (d) Time-dependence of the normalized emission at 6 V as obtained from a KMC degradation study which assumes only TPQ-t processes (see the main text) and which assumes that each quenching is followed by a degradation process upon the involved dye molecule becomes non-emissive. The simulations were carried out with and without exciton diffusion (closed and open symbols, respectively). The dashed curve is a stretched-exponential fit to the simulation results without diffusion (see the main text). Reproduced with permission from Adv. Funct. Mater. (2015), 25, 2024–2037.

polaron involved is displaced to the site at which the triplet exciton resides (a “TPQ-t process”, see Figure 2 in Ref. [CvEJB15]), which then becomes non-emissive with a degradation probability $p_{\text{degr}} = 1$. The simulations thus employ the largest possible acceleration factor. All other parameters are kept identical. The current density was found to remain essentially unchanged during the degradation process. Furthermore, it was found that choosing a smaller degradation probability does not significantly change the results, apart from changing the time scale. That indicates that the lifetime is still much larger than all other relevant time scales. Simulations including exciton diffusion are computationally more expensive, and were stopped when a 50% emission reduction had been obtained. Simulations without diffusion were continued until a reduction to only about 10% of the initial emission was reached. An approximate description of the decay is given by the stretched exponential curve, shown in the figure, with the form $I(t) = I(0) \exp[-(t/\tau_{\text{sim,acc}})^\beta]$, with a simulated accelerated (1/e) lifetime $\tau_{\text{sim,acc}} \cong 80 \mu\text{s}$ and a stretching exponent $\beta = 0.91$. The actual (1/e) lifetime as predicted from the simulations is given by

$$\tau_{\text{sim}} = \frac{\tau_{\text{sim,acc}}}{p_{\text{degr}}}. \quad (1.40)$$

Conversely, using Equation (1.40) the value of p_{degr} could be deduced from a degradation simulation and a measurement of the lifetime. Such an analysis led in Ref. [CvEJB15] to an estimated order-of-magnitude value of $p_{\text{degr}} \sim 10^{-8}$ when assuming that the simulations discussed above are relevant to state-of-the-art white OLEDs.

Within a refined approach, the probability that a TPQ process gives rise to degradation could be treated stochastically, e.g. by treating it as a thermally activated process with an activation energy with a Gaussian distribution. Such an approach is expected to give rise to a smaller value of the stretching exponent β . Experimentally, values of β around 0.5 have been observed. The effect is so far generally explained in a rather phenomenological manner [FRV⁺05]. It should be noted that the decay can also become more stretched-exponential like for OLEDs with imbalanced electron and hole mobilities, resulting in a highly non-uniform emission profile. If this picture is correct, lifetime studies could also, albeit indirectly, provide information about the shape of the emission profile.

We envisage that, using Equation (1.40), lifetime predictions can be obtained from KMC lifetime simulations if the parameter p_{degr} (or its distribution) can be determined from a few well-chosen combined experimental and KMC calibration studies. Subsequently, KMC based lifetime predictions can be obtained for other measurement conditions (e.g. current density and temperature), device architectures, and other dye concentrations in the same host. So far, studies which could validate this view have not been carried out. As a first step, KMC simulations were carried out of the iridium dye concentration dependence of the lifetime, for otherwise identical simulation parameters [CvEJB15]. Figure 1.13(a) shows the accelerated LT_{90} lifetime obtained from the simulations (large open circles), and results from simulations in which exciton diffusion was switched off (small open circles). For iridium dye concentration above about 7 mol%, exciton diffusion is found to yield a significant decrease of the lifetime, up to a factor ~ 4 . The exciton diffusion length is then larger than the average distance to a degraded site, so that a large fraction of the excitons which have been generated on non-degraded sites is lost due to diffusion and subsequent non-radiative decay on degraded sites. Interestingly, the IQE obtained when exciton diffusion was switched off was found to be slightly reduced for all systems studied, namely by 1 – 2%. The reduction cannot be due to switching off the transfer of triplets from matrix to guest sites, as due to the large energy gap of the matrix materials all excitons are generated directly on the dye sites. We surmise that the reduction is due to switching off the possibility that excitons diffuse to molecular sites in regions with a slightly smaller average polaron density, in which the loss due to TPQ is reduced. This effect may for the highest iridium dye concentrations considered be compensated in part by an increase of the IQE due to a smaller exciton diffusion contribution to the TPQ loss. For the devices and the parameter values employed, the latter effect was found

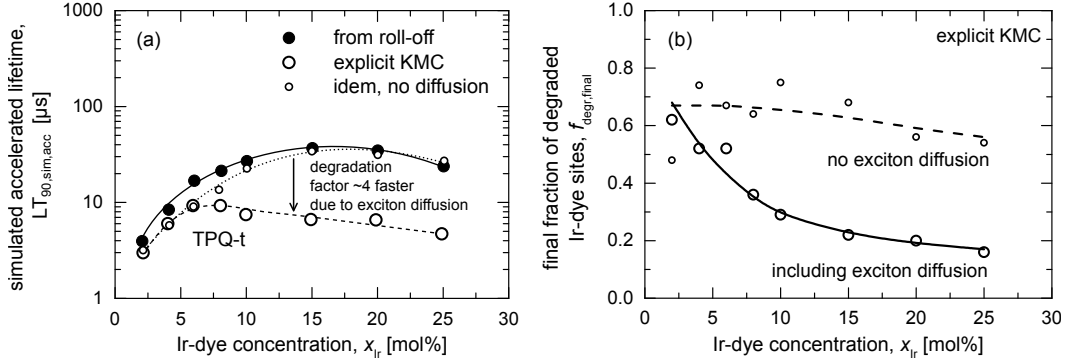


FIGURE 1.13 (a) Ir-dye concentration dependence of the LT_{90} lifetime as obtained from accelerated KMC lifetime simulations for the OLEDs shown in Figure 1.12(a), at 6 V, for the TPQ-t degradation scenario discussed in the main text (large open circles) and when switching off exciton diffusion (small open circles). The closed circles show the accelerated lifetime which is expected from the simulated roll-off using Equation 1.42. The curves are guides-to-the-eye. The predicted actual LT_{90} lifetime is equal to $LT_{90,\text{sim,acc}}/p_{\text{degr}}$, with p_{degr} the probability that upon a TPQ event degradation takes place. Note that due to a variation of the current density with the Ir-dye concentration (see the main text) the lifetime as obtained using Equation 1.42 is not proportional to that concentration. (b) Ir-dye concentration dependence of the fraction of degraded Ir-dye molecules in the $t \rightarrow \infty$ limit, as obtained from the same KMC simulations including and without exciton diffusion. Reproduced with permission from Adv. Funct. Mater. (2015), 25, 2024–2037.

to be almost negligible for iridium dye concentrations around and below 8 mol% [CvEBJ15].

The simulation data shown in Figure 1.13(a) may be analyzed more quantitatively with the help of a useful relationship which has been established between the lifetime and the IQE roll-off [CvEBJ15]. It is based on a model which assumes uniform electron, hole and exciton densities in the emissive layer. If the charge carrier mobility is charge carrier concentration (c) dependent and proportional to c^b , with b a positive exponent which increases with an increasing width of the polaron density of states, the IQE roll-off curve is given by

$$\eta_{\text{IQE}} = \frac{\eta_{\text{rad}}}{1 + \left(\frac{J}{J_{50}}\right)^m}, \quad (1.41)$$

with η_{rad} the PL efficiency (0.75 for the case studied in this section), J_{50} the current density at which the IQE has dropped to 50% of its low-voltage value, and $m = (1 + b)/(2 + b)$. In the absence of exciton diffusion, the simulated accelerated (1/e) lifetime is then given by

$$\tau_{\text{sim,acc}} = edn_{\text{dye}}J_{50}^m/J^{m+1}, \quad (1.42)$$

with d the EML layer thickness and n_{dye} the dye molecule volume density. From this formalism, a current density acceleration exponent $m+1 = (3+2b)/(2+b)$ in the range 1.5 to 2 is expected, as is indeed often observed for phosphorescent OLEDs. The linear n_{dye} dependence is due to the linear increase with increasing dye concentration of the probability that a dye is still emissive after a certain period of operation. The closed circles in Figure 1.13 show the simulated accelerated LT_{90} lifetime, obtained using Equation (1.42) under the assumption of exponential decay ($\beta = 1$), so that $LT_{90,\text{sim,acc}} = -\ln(0.9) \times \tau_{\text{sim,acc}} \cong 0.105 \times \tau_{\text{sim,acc}}$. These predictions from the roll-off curves agree quite well with the explicit KMC simulation results, obtained when exciton diffusion is switched off (small open circles). We note that at the constant voltage (6 V) condition employed, the current density shows a weak but non-negligible non-monotonic dependence on the Ir-dye concentration. It shows a broad minimum around a concentration of approximately

10 mol%, and is $\sim 15\%$ larger for the 2 and 25 mol% systems. Within the concentration range studied, the transport shows a cross-over from a low-concentration guest-host-guest hopping regime, in which the guest molecule states act as traps, to a high-concentration regime, in which the transport is predominantly due to direct guest-guest hopping (see e.g. Figure 5(a) in Ref. [CB12]). The lifetime as obtained using Equation (1.42) is therefore not proportional to the Ir-dye concentration.

Various optical and chemical analytical techniques have been used to investigate the degradation mechanisms of OLEDs and to quantify the concentrations of degraded molecules (see Ref. [SKLL15] and references therein). In future studies, it would be useful to compare such experimental results with the results of KMC simulations. Interestingly, the simulations for the model systems discussed in this section revealed that, to a good approximation, the fraction of degraded Ir-dye molecules increases with time as

$$f_{\text{degr}}(t) = f_{\text{degr,final}} \left[1 - \exp \left(- (t/\tau_{\text{sim,acc}})^\beta \right) \right], \quad (1.43)$$

with $f_{\text{degr,final}}$ the final ($t \rightarrow \infty$) fraction of degraded Ir-dye molecules.

The values of $\tau_{\text{sim,acc}}$ and β are, within the numerical uncertainty, equal to the values describing the luminance decay. Figure 1.13(b) shows the Ir-dye concentration dependence of $f_{\text{degr,final}}$ as obtained from KMC simulations with and without exciton diffusion. The figure shows that in the absence of diffusion, only 60 – 70% of the sites has been degraded in the $t = \infty$ limit. This result indicates that on a significant fraction (30 – 40%) of the sites excitons are either never formed, or that excitons on those sites are well protected against TPQ due to a position of those sites well outside the somewhat filamentary electron and hole current density pathways. The first explanation is consistent with the finding that in systems with a monomodal Gaussian density of states exciton generation preferentially takes place on sites with a low-lying electron or hole state [vdHvOCB09]. When exciton diffusion is included, $f_{\text{degr,final}}$ is found to decrease significantly with increasing Ir-dye concentration, to only approximately 0.16 for 25 mol% systems. This is consistent with the view that due to the energetic disorder the average polaron density and the local polaron diffusivity will be quite non-uniform [vdHUR⁺09, MCB14], so that in the case of strong exciton diffusion degradation will occur predominantly on the relatively small fraction of sites which are located in a region with a large average polaron density and diffusivity.

We emphasize that the degradation scenario assumed in the case study discussed in this section was only chosen for the purpose of giving a demonstration of the feasibility of KMC lifetime simulations. Including monomolecular or other bimolecular scenarios or including refinements (e.g. a degradation probability distribution, conversion of the degraded molecules to polaron trap sites, or an extension of the TPQ interaction range so that the role of the degraded molecule as an exciton quencher is enhanced) is straightforward. It will be also useful to develop analytical models such as discussed above for other degradation scenarios and to extend these to a more realistic non-uniform emission from the EML, in which the lifetime becomes position-dependent, so that the emission decay becomes more stretched-exponential like.

1.13 Outlook

In this chapter we have reviewed multiscale techniques used to simulate organic light emitting diodes and demonstrated the feasibility of full 3D OLED modeling. As an outlook, we would like to mention areas where substantial method development is still required in order to achieve a parameter-free modeling of realistic devices. Refined studies which aim at developing a final view on the detailed performance of specific devices should consider: (i) first-principles evaluations of charge injection rates, (ii) explicit treatment of the induction interaction when solving the master equation, (iii) quantitative treatment of excited states embedded in a heterogeneous

polarizable molecular environment, (iv) more quantitative descriptions of charge–exciton and exciton–exciton interactions, and (v) descriptions of TTA and TPQ as longer-range Förster and Dexter-type interactions. Advancements in all these directions are absolutely vital for devising accurate structure–property relationships for organic semiconductors used in OLEDs.

Acknowledgments

This work was in part supported by the BMBF grants MEDOS (FKZ 03EK3503B), MESOMERIE (FKZ 13N10723), and InterPhase (FKZ 13N13661). The project has received funding from the NMP-20-2014 – “Widening materials models” program under Grant Agreement No. 646259 (MOSTOPHOS). The project was also supported by NanoNextNL, a nanotechnology program of the Dutch ministry of economic affairs. Part of the work of one of the authors (RC) was carried out at the Philips Research Laboratories (Eindhoven, The Netherlands).

References

1. Chihaya Adachi, Marc A. Baldo, Stephen R. Forrest, Sergey Lamansky, Mark E. Thompson, and Raymond C. Kwong. High-efficiency red electrophosphorescence devices. *Appl. Phys. Lett.*, 78(11):1622–1624, 2001.
2. Isamu Akasaki. Nobel Lecture: Fascinated journeys into blue light. *Rev. Mod. Phys.*, 87(4):1119–1131, 2015.
3. Kamal Asadi, Auke J. Kronemeijer, Tobias Cramer, L. Jan Anton Koster, Paul W. M. Blom, and Dago M. de Leeuw. Polaron hopping mediated by nuclear tunnelling in semiconducting polymers at high carrier density. *Nature Communications*, 4:1710, 2013.
4. Stavros Athanasopoulos, James Kirkpatrick, Diego Martinez, Jarvist M. Frost, Clare M. Foden, Alison B. Walker, and Jenny Nelson. Predictive Study of Charge Transport in Disordered Semiconducting Polymers. *Nano Letters*, 7(6):1785–1788, 2007.
5. Hiroshi Amano. Nobel Lecture: Growth of GaN on sapphire via low-temperature deposited buffer layer and realization of p-type GaN by Mg doping followed by low-energy electron beam irradiation. *Rev. Mod. Phys.*, 87(4):1133–1138, 2015.
6. Denis Andrienko. Simulations of Morphology and Charge Transport in Supramolecular Organic Materials. In *Supramolecular Materials for Opto-Electronics*. 2014.
7. Hany Aziz and Zoran D. Popovic. Degradation Phenomena in Small-Molecule Organic Light-Emitting Devices. *Chem. Mater.*, 16(23):4522–4532, 2004.
8. Hany Aziz, Zoran D. Popovic, Nan-Xing Hu, Ah-Mee Hor, and Gu Xu. Degradation Mechanism of Small Molecule-Based Organic Light-Emitting Devices. *Science*, 283(5409):1900–1902, 1999.
9. H. Baessler. Charge Transport in Disordered Organic Photoconductors: a Monte Carlo Simulation Study. *physica status solidi (b)*, 175(1):15–56, 1993.
10. S. D. Baranovskii. Theoretical description of charge transport in disordered organic semiconductors. *physica status solidi (b)*, 251(3):487–525, 2014.
11. Tristan Beraud, Denis Andrienko, and O. Anatole von Lilienfeld. Transferable Atomic Multipole Machine Learning Models for Small Organic Molecules. *J. Chem. Theory. Comput.*, 11(7):3225–3233, 2015.
12. Jean-Luc Bredas, David Beljonne, Veaceslav Coropceanu, and Jerome Cornil. Charge-Transfer and Energy-Transfer Processes in pi-Conjugated Oligomers and Polymers: A Molecular Picture. *Chem. Rev.*, 104(11):4971–5004, 2004.
13. Wolfgang Brütting, Joerg Frischeisen, Tobias D. Schmidt, Bert J. Scholz, and Christian

- Mayr. Device efficiency of organic light-emitting diodes: Progress by improved light outcoupling. *physica status solidi (a)*, 210(1):44–65, 2013.
14. M. Bixon and Joshua Jortner. Electron Transfer—from Isolated Molecules to Biomolecules. In I. Prigogine and Stuart A. Rice, editors, *Advances in Chemical Physics*, pages 35–202. John Wiley & Sons, Inc., 2007.
 15. Bjoern Baumeier, James Kirkpatrick, and Denis Andrienko. Density-functional based determination of intermolecular charge transfer properties for large-scale morphologies. *Phys. Chem. Chem. Phys.*, 12(36):11103, 2010.
 16. V. Bulovi, V. B. Khalfin, G. Gu, P. E. Burrows, D. Z. Garbuzov, and S. R. Forrest. Weak microcavity effects in organic light-emitting devices. *Phys. Rev. B*, 58(7):3730–3740, 1998.
 17. A.B. Bortz, M.H. Kalos, and J.L. Lebowitz. A new algorithm for Monte Carlo simulation of Ising spin systems. *J. Comput. Phys.*, 17(1):10–18, 1975.
 18. M. A. Baldo, S. Lamansky, P. E. Burrows, M. E. Thompson, and S. R. Forrest. Very high-efficiency green organic light-emitting devices based on electrophosphorescence. *Appl. Phys. Lett.*, 75(1):4–6, 1999.
 19. M. Bouhassoune, S.L.M. van Mensfoort, P.A. Bobbert, and R. Coehoorn. Carrier-density and field-dependent charge-carrier mobility in organic semiconductors with correlated Gaussian disorder. *Organic Electronics*, 10(3):437–445, 2009.
 20. Brent H. Besler, Kenneth M. Merz, and Peter A. Kollman. Atomic charges derived from semiempirical methods. *J. Comput. Chem.*, 11(4):431–439, 1990.
 21. Bjoern Baumeier, Ole Stenzel, Carl Poelking, Denis Andrienko, and Volker Schmidt. Stochastic modeling of molecular charge transport networks. *Phys. Rev. B*, 86(18):184202, 2012.
 22. Curt M. Breneman and Kenneth B. Wiberg. Determining atom-centered monopoles from molecular electrostatic potentials. The need for high sampling density in formamide conformational analysis. *J. Comput. Chem.*, 11(3):361–373, 1990.
 23. J. Cottaar and P. A. Bobbert. Calculating charge-carrier mobilities in disordered semiconducting polymers: Mean field and beyond. *Phys. Rev. B*, 74(11):115204, 2006.
 24. R. Coehoorn and P. A. Bobbert. Effects of Gaussian disorder on charge carrier transport and recombination in organic semiconductors. *physica status solidi (a)*, 209(12):2354–2377, 2012.
 25. J. Cottaar, R. Coehoorn, and P. A. Bobbert. Modeling of charge transport across disordered organic heterojunctions. *Organic Electronics*, 13(4):667–672, 2012.
 26. Veaceslav Coropceanu, Jerome Cornil, Demetrio A. da Silva Filho, Yoann Olivier, Robert Silbey, and Jean-Luc Bredas. Charge Transport in Organic Semiconductors. *Chem. Rev.*, 107(4):926–952, 2007.
 27. Reinder Coehoorn, Volker van Elsbergen, and Coen Verschuren. High Efficiency OLEDs for Lighting Applications. In Eugenio Cantatore, editor, *Applications of Organic and Printed Electronics*, Integrated Circuits and Systems, pages 83–100. Springer US, 2013.
 28. R. R. Chance, A. Prock, and R. Silbey. Molecular Fluorescence and Energy Transfer Near Interfaces. In I. Prigogine and Stuart A. Rice, editors, *Advances in Chemical Physics*, pages 1–65. John Wiley & Sons, Inc., 1978.
 29. Reinder Coehoorn, Harm van Eersel, Peter Bobbert, and Ren Janssen. Kinetic Monte Carlo Study of the Sensitivity of OLED Efficiency and Lifetime to Materials Parameters. *Adv. Funct. Mater.*, 25(13):2024–2037, 2015.
 30. Bernard Derrida. Velocity and diffusion constant of a periodic one-dimensional hopping model. *J. Stat. Phys.*, 31(3):433–450, 1983.
 31. D. L. Dexter. A Theory of Sensitized Luminescence in Solids. *J. Chem. Phys.*, 21(5):836–850, 1953.

32. S. W. de Leeuw, J. W. Perram, and E. R. Smith. Simulation of Electrostatic Systems in Periodic Boundary Conditions. I. Lattice Sums and Dielectric Constants. *Proceedings of the Royal Society A: Mathematical, Physical and Engineering Sciences*, 373(1752):27–56, 1980.
33. Kostas Ch Daoulas and Marcus Mller. Comparison of Simulations of Lipid Membranes with Membranes of Block Copolymers. In Wolfgang Peter Meier and Wolfgang Knoll, editors, *Polymer Membranes/Biomembranes*, number 224 in *Advances in Polymer Science*, pages 43–85. Springer Berlin Heidelberg, 2010.
34. J. L. Doob. Topics in the theory of Markoff chains. *Transactions of the American Mathematical Society*, 52(1):37–37, 1942.
35. J. L. Doob. Markoff Chains—Denumerable Case. *Transactions of the American Mathematical Society*, 58(3):455, 1945.
36. D. H. Dunlap, P. E. Parris, and V. M. Kenkre. Charge-Dipole Model for the Universal Field Dependence of Mobilities in Molecularly Doped Polymers. *Phys. Rev. Lett.*, 77(3):542–545, 1996.
37. Peter Deglmann, Ansgar Schaefer, and Christian Lennartz. Application of Quantum Calculations in the Chemical Industry—An Overview. *Int. J. Quantum Chem.*, 115(3):107–136, 2015. WOS:000346654700001.
38. R. J. de Vries, S. L. M. van Mensfoort, R. A. J. Janssen, and R. Coehoorn. Relation between the built-in voltage in organic light-emitting diodes and the zero-field voltage as measured by electroabsorption. *Phys. Rev. B*, 81(12):125203, 2010.
39. Lian Duan, Kai Xie, and Yong Qiu. Review Paper: Progress on efficient cathodes for organic light-emitting diodes. *Journal of the Society for Information Display*, 19(6):453–461, 2011.
40. F. Ercolessi and J. B. Adams. Interatomic Potentials from First-Principles Calculations: The Force-Matching Method. *EPL (Europhysics Letters)*, 26(8):583, 1994.
41. H. van Eersel, P. A. Bobbert, and R. Coehoorn. Kinetic Monte Carlo study of triplet-triplet annihilation in organic phosphorescent emitters. *J. Appl. Phys.*, 117(11):115502, 2015.
42. H. van Eersel, P. A. Bobbert, R. a. J. Janssen, and R. Coehoorn. Monte Carlo study of efficiency roll-off of phosphorescent organic light-emitting diodes: Evidence for dominant role of triplet-polaron quenching. *Appl. Phys. Lett.*, 105(14):143303, 2014.
43. Reinhold Egger, C. H. Mak, and Ulrich Weiss. Quantum rates for nonadiabatic electron transfer. *J. Chem. Phys.*, 100(4):2651–2660, 1994.
44. P. P. Ewald. Die Berechnung optischer und elektrostatischer Gitterpotentiale. *Annalen der Physik*, 369(3):253–287, 1921.
45. Richard Friend, Jeremy Burroughes, and Donal Bradley. *Electroluminescent Devices*, 1990.
46. Matthew P. A. Fisher and Alan T. Dorsey. Dissipative Quantum Tunneling in a Biased Double-Well System at Finite Temperatures. *Phys. Rev. Lett.*, 54(15):1609–1612, 1985.
47. Akio Fukase, Kinh Luan Thanh Dao, and Junji Kido. High-efficiency organic electroluminescent devices using iridium complex emitter and arylamine-containing polymer buffer layer. *Polymers for Advanced Technologies*, 13(8):601–604, 2002.
48. Michael Flaemmich, Dirk Michaelis, and Norbert Danz. Accessing OLED emitter properties by radiation pattern analyses. *Organic Electronics*, 12(1):83–91, 2011.
49. Mauro Furno, Rico Meerheim, Simone Hofmann, Bjoern Luessem, and Karl Leo. Efficiency and rate of spontaneous emission in organic electroluminescent devices. *Phys. Rev. B*, 85(11):115205, 2012.
50. Th. Foerster. Zwischenmolekulare Energiewanderung und Fluoreszenz. *Annalen der*

- Physik*, 437(1-2):55–75, 1948.
51. Stephen R. Forrest. The path to ubiquitous and low-cost organic electronic appliances on plastic. *Nature*, 428(6986):911–918, 2004.
 52. Reinhold F. Fink, Johannes Pfister, Hong Mei Zhao, and Bernd Engels. Assessment of quantum chemical methods and basis sets for excitation energy transfer. *Chem. Phys.*, 346(1-3):275–285, 2008. WOS:000256142000032.
 53. C. Fry, B. Racine, D. Vaufrey, H. Doyeux, and S. Cin. Physical mechanism responsible for the stretched exponential decay behavior of aging organic light-emitting diodes. *Appl. Phys. Lett.*, 87(21):213502, 2005.
 54. Andreas Fuchs, Thomas Steinbrecher, Mario S. Mommer, Yuki Nagata, Marcus Elstner, and Christian Lennartz. Molecular origin of differences in hole and electron mobility in amorphous Alq3 - a multiscale simulation study. *Phys. Chem. Chem. Phys.*, 14(12):4259–4270, 2012.
 55. Kristen A. Fichtorn and W. H. Weinberg. Theoretical foundations of dynamical Monte Carlo simulations. *J. Chem. Phys.*, 95(2):1090, 1991.
 56. Joerg Frischeisen, Daisuke Yokoyama, Chihaya Adachi, and Wolfgang Bruetting. Determination of molecular dipole orientation in doped fluorescent organic thin films by photoluminescence measurements. *Appl. Phys. Lett.*, 96(7):073302, 2010.
 57. Michael A. Gibson and Jehoshua Bruck. Efficient Exact Stochastic Simulation of Chemical Systems with Many Species and Many Channels. *J. Phys. Chem. A*, 104(9):1876–1889, 2000.
 58. Brian A. Gregg, Si-Guang Chen, and Russell A. Cormier. Coulomb Forces and Doping in Organic Semiconductors. *Chem. Mater.*, 16(23):4586–4599, 2004.
 59. N. C. Giebink, B. W. D’Andrade, M. S. Weaver, P. B. Mackenzie, J. J. Brown, M. E. Thompson, and S. R. Forrest. Intrinsic luminance loss in phosphorescent small-molecule organic light emitting devices due to bimolecular annihilation reactions. *J. Appl. Phys.*, 103(4):044509, 2008.
 60. N. C. Giebink and S. R. Forrest. Quantum efficiency roll-off at high brightness in fluorescent and phosphorescent organic light emitting diodes. *Phys. Rev. B*, 77(23):235215, 2008.
 61. Daniel T Gillespie. A general method for numerically simulating the stochastic time evolution of coupled chemical reactions. *J. Comput. Phys.*, 22(4):403–434, 1976.
 62. Daniel T. Gillespie. Exact stochastic simulation of coupled chemical reactions. *J. Phys. Chem.*, 81(25):2340–2361, 1977.
 63. Patrick Gemnden, Carl Poelking, Kurt Kremer, Denis Andrienko, and Kostas Ch. Daoulas. Nematic Ordering, Conjugation, and Density of States of Soluble Polymeric Semiconductors. *Macromolecules*, 46(14):5762–5774, 2013.
 64. Patrick Gemnden, Carl Poelking, Kurt Kremer, Kostas Daoulas, and Denis Andrienko. Effect of Mesoscale Ordering on the Density of States of Polymeric Semiconductors. *Macromol. Rapid Commun.*, 36(11):1047–1053, 2015.
 65. Malte C. Gather and Sebastian Reineke. Recent advances in light outcoupling from white organic light-emitting diodes. *Journal of Photonics for Energy*, 5(1):057607–057607, 2015.
 66. H.K. Gummel. A self-consistent iterative scheme for one-dimensional steady state transistor calculations. *IEEE Transactions on Electron Devices*, 11(10):455–465, 1964.
 67. W. Chr. Germs, J. J. M. van der Holst, S. L. M. van Mensfoort, P. A. Bobbert, and R. Coehoorn. Modeling of the transient mobility in disordered organic semiconductors with a Gaussian density of states. *Phys. Rev. B*, 84(16):165210, 2011.
 68. Fruzsina Gajdos, Siim Valner, Felix Hoffmann, Jacob Spencer, Marian Breuer, Adam Kubas, Michel Dupuis, and Jochen Blumberger. Ultrafast estimation of electronic couplings for electron transfer between pi-conjugated organic molecules. *J. Chem.*

Theory. Comput., 2014.

69. Hermann Grabert and Ulrich Weiss. Quantum Tunneling Rates for Asymmetric Double-Well Systems with Ohmic Dissipation. *Phys. Rev. Lett.*, 54(15):1605–1608, 1985.
70. Mario Heidernaetsch, Michael Bauer, and Guenter Radons. Characterizing N-dimensional anisotropic Brownian motion by the distribution of diffusivities. *J. Chem. Phys.*, 139(18):184105, 2013.
71. R.L. Henderson. A uniqueness theorem for fluid pair correlation functions. *Physics Letters A*, 49(3):197–198, 1974.
72. Jingsong Huang and Miklos Kertesz. Validation of intermolecular transfer integral and bandwidth calculations for organic molecular materials. *J. Chem. Phys.*, 122(23):234707, 2005.
73. Josef Honerkamp. *Stochastische dynamische Systeme : Konzepte, numerische Methoden, Datenanalysen*. VCH, Weinheim [u.a.], 1990.
74. Geoffrey R. Hutchison, Mark A. Ratner, and Tobin J. Marks. Hopping Transport in Conductive Heterocyclic Oligomers: Reorganization Energies and Substituent Effects. *J. Am. Chem. Soc.*, 127(7):2339–2350, 2005.
75. Richard D. Harcourt, Gregory D. Scholes, and Kenneth P. Ghiggino. Rate expressions for excitation transfer. II. Electronic considerations of direct and through configuration exciton resonance interactions. *J. Chem. Phys.*, 101(12):10521–10525, 1994.
76. Shuzo Hirata, Yumi Sakai, Kensuke Masui, Hiroyuki Tanaka, Sae Youn Lee, Hiroko Nomura, Nozomi Nakamura, Mao Yasumatsu, Hajime Nakanotani, Qisheng Zhang, Katsuyuki Shizu, Hiroshi Miyazaki, and Chihaya Adachi. Highly efficient blue electroluminescence based on thermally activated delayed fluorescence. *Nat. Mater.*, 14(3):330–336, 2015.
77. S. Izvekov, M. Parrinello, C. J Burnham, and G. A Voth. Effective force fields for condensed phase systems from ab initio molecular dynamics simulation: A new method for force-matching. *J. Chem. Phys.*, 120(23):10896–10913, 2004.
78. Mara Jochum, Denis Andrienko, Kurt Kremer, and Christine Peter. Structure-based coarse-graining in liquid slabs. *J. Chem. Phys.*, 137(6):064102, 2012.
79. A.P.J. Jansen. Monte Carlo simulations of chemical reactions on a surface with time-dependent reaction-rate constants. *Computer Physics Communications*, 86(1-2):1–12, 1995.
80. William L. Jorgensen, David S. Maxwell, and Julian Tirado-Rives. Development and Testing of the OPLS All-Atom Force Field on Conformational Energetics and Properties of Organic Liquids. *J. Am. Chem. Soc.*, 118(45):11225–11236, 1996.
81. William L. Jorgensen and Julian Tirado-Rives. The OPLS [optimized potentials for liquid simulations] potential functions for proteins, energy minimizations for crystals of cyclic peptides and crambin. *J. Am. Chem. Soc.*, 110(6):1657–1666, 1988.
82. Pascal Kordt and Denis Andrienko. Modeling of Spatially Correlated Energetic Disorder in Organic Semiconductors. *J. Chem. Theory. Comput.*, 12(1):36–40, 2016.
83. Yuichiro Kawamura, Jason Brooks, Julie J. Brown, Hiroyuki Sasabe, and Chihaya Adachi. Intermolecular Interaction and a Concentration-Quenching Mechanism of Phosphorescent Ir(III) Complexes in a Solid Film. *Phys. Rev. Lett.*, 96(1):017404, 2006.
84. Chan Hyung Kim, Chang Deuck Bae, Kyung Hee Ryu, Bong Ki Lee, and Hyun Jung Shin. Local Work Function Measurements on Various Inorganic Materials Using Kelvin Probe Force Spectroscopy. *Solid State Phenomena*, 124-126:607–610, 2007.
85. Adam Kubas, Felix Hoffmann, Alexander Heck, Harald Oberhofer, Marcus Elstner, and Jochen Blumberger. Electronic couplings for molecular charge transfer: Benchmarking CDFT, FODFT, and FODFTB against high-level ab initio calculations.

- J. Chem. Phys.*, 140(10):104105, 2014.
86. E. Knapp, R. Husermann, H. U. Schwarzenbach, and B. Ruhstaller. Numerical simulation of charge transport in disordered organic semiconductor devices. *J. Appl. Phys.*, 108(5):054504, 2010.
 87. James Kirkpatrick. An approximate method for calculating transfer integrals based on the ZINDO Hamiltonian. *Int. J. Quantum Chem.*, 108(1):51–56, 2008.
 88. Sei-Yong Kim and Jang-Joo Kim. Outcoupling efficiency of organic light emitting diodes and the effect of ITO thickness. *Organic Electronics*, 11(6):1010–1015, 2010.
 89. D. Y. Kondakov, W. C. Lenhart, and W. F. Nichols. Operational degradation of organic light-emitting diodes: Mechanism and identification of chemical products. *J. Appl. Phys.*, 101(2):024512, 2007.
 90. James Kirkpatrick, Valentina Marcon, Jenny Nelson, Kurt Kremer, and Denis Andrienko. Charge Mobility of Discotic Mesophases: A Multiscale Quantum and Classical Study. *Phys. Rev. Lett.*, 98(22):227402, 2007.
 91. G. Kaniadakis and P. Quarati. Kinetic equation for classical particles obeying an exclusion principle. *Phys. Rev. E*, 48(6):4263–4270, 1993.
 92. Evelyne Knapp and Beat Ruhstaller. Numerical impedance analysis for organic semiconductors with exponential distribution of localized states. *Appl. Phys. Lett.*, 99(9):–, 2011.
 93. Pascal Kordt, Ole Stenzel, Bjoern Baumeier, Volker Schmidt, and Denis Andrienko. Parametrization of Extended Gaussian Disorder Models from Microscopic Charge Transport Simulations. *J. Chem. Theory. Comput.*, 10(6):2508–2513, 2014.
 94. Pascal Kordt, Sven Stodtmann, Alexander Badinski, Mustapha Al Helwi, Christian Lennartz, and Denis Andrienko. Parameter-free continuous drift-diffusion models of amorphous organic semiconductors. *Phys. Chem. Chem. Phys.*, 17(35):22778–22783, 2015.
 95. Pascal Kordt, Jeroen J. M. van der Holst, Mustapha Al Helwi, Wolfgang Kowalsky, Falk May, Alexander Badinski, Christian Lennartz, and Denis Andrienko. Modeling of Organic Light Emitting Diodes: From Molecular to Device Properties. *Adv. Funct. Mater.*, 25(13):1955–1971, 2015.
 96. Yuichiro Kawamura, Shozo Yanagida, and Stephen R. Forrest. Energy transfer in polymer electrophosphorescent light emitting devices with single and multiple doped luminescent layers. *J. Appl. Phys.*, 92(1):87–93, 2002.
 97. Alexander Lukyanov and Denis Andrienko. Extracting nondispersive charge carrier mobilities of organic semiconductors from simulations of small systems. *Phys. Rev. B*, 82(19):193202, 2010.
 98. Guglielmo Lanzani. *The photophysics behind photovoltaics and photonics*. Wiley-VCH, Weinheim, 2012. OCLC: ocn768072884.
 99. A. J. Leggett, S. Chakravarty, A. T. Dorsey, Matthew P. A. Fisher, Anupam Garg, and W. Zwerger. Dynamics of the dissipative two-state system. *Rev. Mod. Phys.*, 59(1):1–85, 1987.
 100. Frederic Laquai and Dirk Hertel. Influence of hole transport units on the efficiency of polymer light emitting diodes. *Appl. Phys. Lett.*, 90(14):142109, 2007.
 101. David R. Lide. *CRC Handbook of Chemistry and Physics, 79th ed.: A Ready-Reference Book of Chemical and Physical Data*. Crc Press, auflage: 79th edition, 1998.
 102. G. Li, C. H. Kim, Z. Zhou, J. Shinar, K. Okumoto, and Y. Shirota. Combinatorial study of exciplex formation at the interface between two wide band gap organic semiconductors. *Appl. Phys. Lett.*, 88(25):253505, 2006.
 103. Alexander P. Lyubartsev and Aatto Laaksonen. Calculation of effective interaction potentials from radial distribution functions: A reverse Monte Carlo approach. *Phys. Rev. E*, 52(4):3730–3737, 1995.

104. Alexander Lukyanov, Christian Lennartz, and Denis Andrienko. Amorphous films of tris(8-hydroxyquinolino)aluminium: Force-field, morphology, and charge transport. *physica status solidi (a)*, 206(12):2737–2742, 2009.
105. Jeong-Hwan Lee, Sunghun Lee, Seung-Jun Yoo, Kwon-Hyeon Kim, and Jang-Joo Kim. Langevin and Trap-Assisted Recombination in Phosphorescent Organic Light Emitting Diodes. *Adv. Funct. Mater.*, 24(29):4681–4688, 2014.
106. Girish Lakhwani, Akshay Rao, and Richard H. Friend. Bimolecular Recombination in Organic Photovoltaics. *Annual Review of Physical Chemistry*, 65(1):557–581, 2014.
107. Boris D Lubachevsky. Efficient parallel simulations of dynamic Ising spin systems. *J. Comput. Phys.*, 75(1):103–122, 1988.
108. Allen Miller and Elihu Abrahams. Impurity Conduction at Low Concentrations. *Phys. Rev.*, 120(3):745–755, 1960.
109. Falk May, Mustapha Al-Helwi, Bjoern Baumeier, Wolfgang Kowalsky, Evelyn Fuchs, Christian Lennartz, and Denis Andrienko. Design Rules for Charge-Transport Efficient Host Materials for Phosphorescent Organic Light-Emitting Diodes. *J. Am. Chem. Soc.*, 134(33):13818–13822, 2012. WOS:000307699000042.
110. Rudolph A. Marcus. Electron transfer reactions in chemistry. Theory and experiment. *Rev. Mod. Phys.*, 65(3):599–610, 1993.
111. Falk May, Bjoern Baumeier, Christian Lennartz, and Denis Andrienko. Can Lattice Models Predict the Density of States of Amorphous Organic Semiconductors? *Phys. Rev. Lett.*, 109(13):136401, 2012.
112. Teemu Murtola, Alex Bunker, Ilpo Vattulainen, Markus Deserno, and Mikko Karttunen. Multiscale modeling of emergent materials: biological and soft matter. *Phys. Chem. Chem. Phys.*, 11(12):1869–1892, 2009.
113. A. Mass, R. Coehoorn, and P. A. Bobbert. Universal Size-Dependent Conductance Fluctuations in Disordered Organic Semiconductors. *Phys. Rev. Lett.*, 113(11), 2014.
114. M. Mesta, J. Cottaar, R. Coehoorn, and P. A. Bobbert. Study of charge-carrier relaxation in a disordered organic semiconductor by simulating impedance spectroscopy. *Appl. Phys. Lett.*, 104(21), 2014.
115. Murat Mesta, Marco Carvelli, Rein J. de Vries, Harm van Eersel, Jeroen J. M. van der Holst, Matthias Schober, Mauro Furno, Bjoern Luessem, Karl Leo, Peter Loebel, Reinder Coehoorn, and Peter A. Bobbert. Molecular-scale simulation of electroluminescence in a multilayer white organic light-emitting diode. *Nat. Mater.*, 12(7):652–658, 2013.
116. S. L. M. van Mensfoort, M. Carvelli, M. Megens, D. Wehenkel, M. Bartyzel, H. Greiner, R. A. J. Janssen, and R. Coehoorn. Measuring the light emission profile in organic light-emitting diodes with nanometre spatial resolution. *Nat. Photonics*, 4(0):329–335, 2010.
117. M. M. Mandoc, B. de Boer, G. Paasch, and P. W. M. Blom. Trap-limited electron transport in disordered semiconducting polymers. *Phys. Rev. B*, 75(19):193202, 2007.
118. Ron Mertens. Continental shows a prototype dual-screen flexible AMOLED display for the automotive market — OLED-Info, 2014.
119. Michael Merrick and Kristen A. Fichtorn. Synchronous relaxation algorithm for parallel kinetic Monte Carlo simulations of thin film growth. *Phys. Rev. E*, 75(1), 2007.
120. Volkhard May and Oliver Kuehn. *Charge and Energy Transfer Dynamics in Molecular Systems*. Wiley-VCH, 3rd, revised and enlarged edition edition, 2011.
121. Caroline Murawski, Karl Leo, and Malte C. Gather. Efficiency Roll-Off in Organic Light-Emitting Diodes. *Adv. Mater.*, 25(47):6801–6827, 2013.
122. E. Martnez, J. Marian, M.H. Kalos, and J.M. Perlado. Synchronous parallel ki-

- netic Monte Carlo for continuum diffusion-reaction systems. *J. Comput. Phys.*, 227(8):3804–3823, 2008.
123. K.d. Meisel, W.f. Pasveer, J. Cottaar, C. Tanase, R. Coehoorn, P.a. Bobbert, P.w.m. Blom, D.m. de Leeuw, and M.a.j. Michels. Charge-carrier mobilities in disordered semiconducting polymers: effects of carrier density and electric field. *physica status solidi (c)*, 3(2):267–270, 2006.
 124. Saso Mladenovski, Sebastian Reineke, and Kristiaan Neyts. Measurement and simulation of exciton decay times in organic light-emitting devices with different layer structures. *Opt. Lett.*, 34(9):1375–1377, 2009.
 125. Alston J. Misquitta and Anthony J. Stone. Distributed polarizabilities obtained using a constrained density-fitting algorithm. *J. Chem. Phys.*, 124(2):024111, 2006.
 126. M. Mesta, C. Schaefer, J. de Groot, J. Cottaar, R. Coehoorn, and P. A. Bobbert. Charge-carrier relaxation in disordered organic semiconductors studied by dark injection: Experiment and modeling. *Phys. Rev. B*, 88(17):174204, 2013.
 127. M. Moral, W.-J. Son, J. C. Sancho-Garca, Y. Olivier, and L. Muccioli. Cost-Effective Force Field Tailored for Solid-Phase Simulations of OLED Materials. *J. Chem. Theory. Comput.*, 11(7):3383–3392, 2015.
 128. David P. McMahon and Alessandro Troisi. Evaluation of the External Reorganization Energy of Polyacenes. *J. Phys. Chem. Lett.*, 1(6):941–946, 2010.
 129. Shuji Nakamura. Nobel Lecture: Background story of the invention of efficient blue InGaN light emitting diodes. *Rev. Mod. Phys.*, 87(4):1139–1151, 2015.
 130. Joseph E. Norton and Jean-Luc Bredas. Polarization Energies in Oligoacene Semiconductor Crystals. *J. Am. Chem. Soc.*, 130(37):12377–12384, 2008.
 131. W. G Noid, J. Chu, G. S Ayton, V. Krishna, S. Izvekov, G. A Voth, A. Das, and H. C Andersen. The multiscale coarse graining method. 1. A rigorous bridge between atomistic and coarse-grained models. *J. Chem. Phys.*, 128:244114, 2008.
 132. W. G. Noid, Jih-Wei Chu, Gary S. Ayton, and Gregory A. Voth. Multiscale Coarse-Graining and Structural Correlations: Connections to Liquid-State Theory. *J. Phys. Chem. B*, 111(16):4116–4127, 2007.
 133. S. V. Novikov, D. H. Dunlap, V. M. Kenkre, P. E. Parris, and A. V. Vannikov. Essential Role of Correlations in Governing Charge Transport in Disordered Organic Materials. *Phys. Rev. Lett.*, 81(20):4472–4475, 1998.
 134. Tobias Neumann, Denis Danilov, Christian Lennartz, and Wolfgang Wenzel. Modeling disordered morphologies in organic semiconductors. *J. Comput. Chem.*, 34(31):2716–2725, 2013. bibtex: neumann`modeling`2013.
 135. Kristiaan A. Neyts. Simulation of light emission from thin-film microcavities. *JOSA A*, 15(4):962–971, 1998.
 136. Md. K. Nazeeruddin, R. Humphry-Baker, D. Berner, S. Rivier, L. Zuppiroli, and M. Graetzel. Highly Phosphorescence Iridium Complexes and Their Application in Organic Light-Emitting Devices. *J. Am. Chem. Soc.*, 125(29):8790–8797, 2003.
 137. Jenny Nelson, Joe J. Kwiatkowski, James Kirkpatrick, and Jarvist M. Frost. Modeling Charge Transport in Organic Photovoltaic Materials. *Accounts Chem. Res.*, 42(11):1768–1778, 2009.
 138. Yuki Nagata and Christian Lennartz. Atomistic simulation on charge mobility of amorphous tris(8-hydroxyquinoline) aluminum (Alq₃): Origin of Poole-Frenkel type behavior. *J. Chem. Phys.*, 129(3):034709, 2008.
 139. W. G. Noid. Perspective: Coarse-grained models for biomolecular systems. *J. Chem. Phys.*, 139(9):090901, 2013.
 140. Sergey V. Novikov and Anatoly V. Vannikov. Cluster Structure in the Distribution of the Electrostatic Potential in a Lattice of Randomly Oriented Dipoles. *J. Phys. Chem.*, 99(40):14573–14576, 1995.

141. Roberto Olivares-Amaya, Carlos Amador-Bedolla, Johannes Hachmann, Sule Atahan-Evrenk, Roel S. Sanchez-Carrera, Leslie Vogt, and Aln Aspuru-Guzik. Accelerated computational discovery of high-performance materials for organic photovoltaics by means of cheminformatics. *Energy & Environmental Science*, 4(12):4849–4861, 2011.
142. Woong-Kyo Oh, Shahzada Qamar Hussain, Youn-Jung Lee, Youngseok Lee, Shihyun Ahn, and Junsin Yi. Study on the ITO work function and hole injection barrier at the interface of ITO/a-Si:H(p) in amorphous/crystalline silicon heterojunction solar cells. *Materials Research Bulletin*, 47(10):3032–3035, 2012.
143. Selina Olthof, Shafiqh Mehraeen, Swagat K. Mohapatra, Stephen Barlow, Veaceslav Coropceanu, Jean-Luc Bredas, Seth R. Marder, and Antoine Kahn. Ultralow Doping in Organic Semiconductors: Evidence of Trap Filling. *Phys. Rev. Lett.*, 109(17):176601, 2012.
144. Takuya Otani. Samsung shows new 4" flexible AMOLED that is so thin (0.05mm) it 'flaps' in the wind textbar OLED-Info. 2008.
145. Carl Poelking and Denis Andrienko. Design Rules for Organic Donor-Acceptor Heterojunctions: Pathway for Charge Splitting and Detrapping. *J. Am. Chem. Soc.*, pages 6320–6326, 2015.
146. Carl Poelking and Denis Andrienko. Long-range embedding of molecular ions and excitations in a polarizable molecular environment. 2016.
147. Jin-Seong Park, Heeyeop Chae, Ho Kyoong Chung, and Sang In Lee. Thin film encapsulation for flexible AM-OLED: a review. *Semiconductor Science and Technology*, 26(3):034001, 2011.
148. W. F. Pasveer, J. Cottaar, C. Tanase, R. Coehoorn, P. A. Bobbert, P. W. M. Blom, D. M. de Leeuw, and M. A. J. Michels. Unified Description of Charge-Carrier Mobilities in Disordered Semiconducting Polymers. *Phys. Rev. Lett.*, 94(20), 2005.
149. Carl Poelking, Kostas Daoulas, Alessandro Troisi, and Denis Andrienko. Morphology and Charge Transport in P3ht: A Theorist's Perspective. In Sabine Ludwigs, editor, *P3HT Revisited – From Molecular Scale to Solar Cell Devices*, number 265 in *Advances in Polymer Science*, pages 139–180. Springer Berlin Heidelberg, 2014. DOI: 10.1007/12'2014'277.
150. Qiming Peng, Weijun Li, Shitong Zhang, Ping Chen, Feng Li, and Yuguang Ma. Evidence of the Reverse Intersystem Crossing in Intra-Molecular Charge-Transfer Fluorescence-Based Organic Light-Emitting Devices Through Magneto-Electroluminescence Measurements. *Advanced Optical Materials*, 1(5):362–366, 2013.
151. B. Perucco, N.A. Reinke, D. Rezzonico, E. Knapp, S. Harkema, and B. Ruhstaller. On the exciton profile in OLEDs-seamless optical and electrical modeling. *Organic Electronics*, 13(10):1827–1835, 2012.
152. Carl Poelking, Max Tietze, Chris Elschner, Selina Olthof, Dirk Hertel, Björn Baumeier, Frank Wrthner, Klaus Meerholz, Karl Leo, and Denis Andrienko. Impact of mesoscale order on open-circuit voltage in organic solar cells. *Nat. Mater.*, 14(4):434–439, 2014.
153. Jeffrey R. Reimers. A practical method for the use of curvilinear coordinates in calculations of normal-mode-projected displacements and Duschinsky rotation matrices for large molecules. *J. Chem. Phys.*, 115(20):9103–9109, 2001.
154. Victor Rhle, Christoph Junghans, Alexander Lukyanov, Kurt Kremer, and Denis Andrienko. Versatile Object-Oriented Toolkit for Coarse-Graining Applications. *J. Chem. Theory. Comput.*, 5(12):3211–3223, 2009.
155. Beat Ruhstaller, Evelyne Knapp, Benjamin Perucco, Nils Reinke, Daniele Rezzonico, and Felix Mueller. Advanced Numerical Simulation of Organic Light-emitting Devices.

- In Oleg Sergiyenko, editor, *Optoelectronic Devices and Properties*. InTech, 2011.
156. Victor Rhle, Alexander Lukyanov, Falk May, Manuel Schrader, Thorsten Vehoff, James Kirkpatrick, Bjoern Baumeier, and Denis Andrienko. Microscopic Simulations of Charge Transport in Disordered Organic Semiconductors. *J. Chem. Theory. Comput.*, 7(10):3335–3345, 2011.
 157. Dirk Reith, Mathias Ptz, and Florian Mller-Plathe. Deriving effective mesoscale potentials from atomistic simulations. *J. Comput. Chem.*, 24(13):1624–1636, 2003.
 158. Noam Rappaport, Yevgeni Preezant, and Nir Tessler. Spatially dispersive transport: A mesoscopic phenomenon in disordered organic semiconductors. *Phys. Rev. B*, 76(23):235323, 2007.
 159. Yohai Roichman and Nir Tessler. Generalized Einstein relation for disordered semiconductors-implications for device performance. *Appl. Phys. Lett.*, 80(11):1948–1950, 2002.
 160. Sebastian Reineke, Karsten Walzer, and Karl Leo. Triplet-exciton quenching in organic phosphorescent light-emitting diodes with Ir-based emitters. *Phys. Rev. B*, 75(12):125328, 2007.
 161. Joan Ridley and Michael Zerner. An intermediate neglect of differential overlap technique for spectroscopy: Pyrrole and the azines. *Theoretica Chimica Acta*, 32(2):111–134, 1973.
 162. Yunsic Shim and Jacques G. Amar. Semirigorous synchronous sublattice algorithm for parallel kinetic Monte Carlo simulations of thin film growth. *Phys. Rev. B*, 71(12), 2005.
 163. D.L. Scharfetter and H.K. Gummel. Large-signal analysis of a silicon Read diode oscillator. *IEEE Transactions on Electron Devices*, 16(1):64–77, 1969.
 164. Gregory D. Scholes and Kenneth P. Ghiggino. Rate expressions for excitation transfer I. Radiationless transition theory perspective. *J. Chem. Phys.*, 101(2):1251–1261, 1994.
 165. Yufei Shen and Noel C. Giebink. Monte Carlo Simulations of Nanoscale Electrical Inhomogeneity in Organic Light-Emitting Diodes and Its Impact on Their Efficiency and Lifetime. *Physical Review Applied*, 4(5):054017, 2015.
 166. M. Scott Shell. The relative entropy is fundamental to multiscale and inverse thermodynamic problems. *J. Chem. Phys.*, 129(14):144108, 2008.
 167. Gregory D. Scholes, Richard D. Harcourt, and Kenneth P. Ghiggino. Rate expressions for excitation transfer. III. An ab initio study of electronic factors in excitation transfer and exciton resonance interactions. *J. Chem. Phys.*, 102(24):9574–9581, 1995.
 168. Tobias D. Schmidt, Lars Jaeger, Yutaka Noguchi, Hisao Ishii, and Wolfgang Bruetting. Analyzing degradation effects of organic light-emitting diodes via transient optical and electrical measurements. *J. Appl. Phys.*, 117(21):215502, 2015.
 169. Franky So and Denis Kondakov. Degradation Mechanisms in Small-Molecule and Polymer Organic Light-Emitting Diodes. *Adv. Mater.*, 22(34):3762–3777, 2010.
 170. Frank S. Steinbacher, Ralf Krause, Arvid Hunze, and Albrecht Winnacker. Triplet exciton transfer mechanism between phosphorescent organic dye molecules. *Phys. Stat. Sol. (a)*, 209(2):340–346, 2012.
 171. Sebastian Scholz, Denis Kondakov, Bjoern Luessem, and Karl Leo. Degradation Mechanisms and Reactions in Organic Light-Emitting Devices. *Chem. Rev.*, 115(16):8449–8503, 2015.
 172. R Schlaf, H Murata, and Z. H Kafafi. Work function measurements on indium tin oxide films. *Journal of Electron Spectroscopy and Related Phenomena*, 120(1-3):149–154, 2001.
 173. A. K. Soper. Empirical potential Monte Carlo simulation of fluid structure. *Chem.*

- Phys.*, 202(2~3):295–306, 1996.
174. Shammai Speiser. Photophysics and Mechanisms of Intramolecular Electronic Energy Transfer in Bichromophoric Molecular Systems: Solution and Supersonic Jet Studies. *Chem. Rev.*, 96(6):1953–1976, 1996.
 175. Gregor Schwartz, Sebastian Reineke, Thomas Conrad Rosenow, Karsten Walzer, and Karl Leo. Triplet Harvesting in Hybrid White Organic Light-Emitting Diodes. *Adv. Funct. Mater.*, 19(9):1319–1333, 2009.
 176. Tobias D. Schmidt, Daniel S. Setz, Michael Flaemmich, Joerg Frischeisen, Dirk Michaelis, Benjamin C. Krummacher, Norbert Danz, and Wolfgang Bruetting. Evidence for non-isotropic emitter orientation in a red phosphorescent organic light-emitting diode and its implications for determining the emitter’s radiative quantum efficiency. *Appl. Phys. Lett.*, 99(16):163302, 2011.
 177. Ruben Seifert, Sebastian Scholz, Bjoern Luessem, and Karl Leo. Comparison of ultraviolet- and charge-induced degradation phenomena in blue fluorescent organic light emitting diodes. *Appl. Phys. Lett.*, 97(1):013308, 2010.
 178. Kazuhiko Seki and M. Tachiya. Electric field dependence of charge mobility in energetically disordered materials: Polaron aspects. *Phys. Rev. B*, 65:014305, 2001.
 179. A.J. Stone. Distributed polarizabilities. *Molecular Physics*, 56(5):1065–1082, 1985.
 180. A. J Stone. *The Theory of intermolecular forces*. Clarendon Press, Oxford, 1997.
 181. Anthony J. Stone. Distributed Multipole Analysis - Stability for Large Basis Sets. *J. Chem. Theory. Comput.*, 1(6):1128–1132, 2005.
 182. Eduard Tuti, Ivo Batisti, and Detlef Berner. Injection and strong current channeling in organic disordered media. *Phys. Rev. B*, 70(16):161202, 2004.
 183. C. Tanase, P. W. M. Blom, D. M. de Leeuw, and E. J. Meijer. Charge carrier density dependence of the hole mobility in poly(p-phenylene vinylene). *physica status solidi (a)*, 201(6):1236–1245, 2004.
 184. B.T. Thole. Molecular polarizabilities calculated with a modified dipole interaction. *Chem. Phys.*, 59(3):341–350, 1981.
 185. W. Tschoep, K. Kremer, J. Batoulis, T. Buerger, and O. Hahn. Simulation of polymer melts. I. Coarse-graining procedure for polycarbonates. *Acta Polymerica*, 49(2-3):61–74, 1998.
 186. Kuo-Chun Tang, Kuan Lin Liu, and I-Chia Chen. Rapid intersystem crossing in highly phosphorescent iridium complexes. *Chem. Phys. Lett.*, 386(4-6):437 – 441, 2004.
 187. C. W. Tang and S. A. VanSlyke. Organic electroluminescent diodes. *Appl. Phys. Lett.*, 51(12):913–915, 1987.
 188. Edward F. Valeev, Veaceslav Coropceanu, Demetrio A. da Silva Filho, Seyhan Salman, and Jean-Luc Bredas. Effect of Electronic Polarization on Charge-Transport Parameters in Molecular Organic Semiconductors. *J. Am. Chem. Soc.*, 128(30):9882–9886, 2006.
 189. J. J. M. van der Holst, M. A. Uijttewaal, B. Ramachandhran, R. Coehoorn, P. A. Bobbert, G. A. de Wijs, and R. A. de Groot. Modeling and analysis of the three-dimensional current density in sandwich-type single-carrier devices of disordered organic semiconductors. *Phys. Rev. B*, 79(8):085203, 2009.
 190. J. J. M. van der Holst, F. W. A. van Oost, R. Coehoorn, and P. A. Bobbert. Electron-hole recombination in disordered organic semiconductors: Validity of the Langevin formula. *Phys. Rev. B*, 80(23), 2009.
 191. J. J. M. van der Holst, F. W. A. van Oost, R. Coehoorn, and P. A. Bobbert. Monte Carlo study of charge transport in organic sandwich-type single-carrier devices: Effects of Coulomb interactions. *Phys. Rev. B*, 83(8):085206, 2011.
 192. N.J. van der Kaap and L.J.A. Koster. Massively parallel kinetic Monte Carlo simulations of charge carrier transport in organic semiconductors. *J. Comput. Phys.*, 307:321–

- 332, 2016.
193. O. Anatole von Lilienfeld, Ivano Tavernelli, Ursula Rothlisberger, and Daniel Sebastiani. Optimization of Effective Atom Centered Potentials for London Dispersion Forces in Density Functional Theory. *Phys. Rev. Lett.*, 93(15):153004, 2004.
 194. S. L. M. van Mensfoort and R. Coehoorn. Determination of Injection Barriers in Organic Semiconductor Devices from Capacitance Measurements. *Phys. Rev. Lett.*, 100(8):086802, 2008.
 195. S. L. M. van Mensfoort and R. Coehoorn. Effect of Gaussian disorder on the voltage dependence of the current density in sandwich-type devices based on organic semiconductors. *Phys. Rev. B*, 78(8):085207, 2008.
 196. S. L. M. van Mensfoort, R. J. de Vries, V. Shabro, H. P. Loebel, R. A. J. Janssen, and R. Coehoorn. Electron transport in the organic small-molecule material BAQ - the role of correlated disorder and traps. *Organic Electronics*, 11(8):1408–1413, 2010.
 197. S. L. M. van Mensfoort, S. I. E. Vulto, R. A. J. Janssen, and R. Coehoorn. Hole transport in polyfluorene-based sandwich-type devices: Quantitative analysis of the role of energetic disorder. *Phys. Rev. B*, 78(8):085208, 2008.
 198. Troy Van Voorhis, Tim Kowalczyk, Benjamin Kaduk, Lee-Ping Wang, Chiao-Lun Cheng, and Qin Wu. The Diabatic Picture of Electron Transfer, Reaction Barriers, and Molecular Dynamics. *Annual Review of Physical Chemistry*, 61(1):149–170, 2010.
 199. Gert-Jan A H Wetzelaer and Paul W M Blom. Diffusion-driven currents in organic-semiconductor diodes. *NPG Asia Materials*, 6(7):e110, 2014.
 200. Z. B. Wang, M. G. Helander, X. F. Xu, D. P. Puzzo, J. Qiu, M. T. Greiner, and Z. H. Lu. Optical design of organic light emitting diodes. *J. Appl. Phys.*, 109(5):053107, 2011.
 201. G. M. Wu, H. H. Lin, and H. C. Lu. Work function and valence band structure of tin-doped indium oxide thin films for OLEDs. *Vacuum*, 82(12):1371–1374, 2008.
 202. K. Walzer, B. Maennig, M. Pfeiffer, and K. Leo. Highly Efficient Organic Devices Based on Electrically Doped Transport Layers. *Chem. Rev.*, 107(4):1233–1271, 2007.
 203. W M Young and E W Elcock. Monte Carlo studies of vacancy migration in binary ordered alloys: I. *Proceedings of the Physical Society*, 89(3):735–746, 1966.
 204. Hartmut Yersin. Triplet Emitters for OLED Applications. Mechanisms of Exciton Trapping and Control of Emission Properties. In *Transition Metal and Rare Earth Compounds*, number 241 in Topics in Current Chemistry, pages 1–26. Springer Berlin Heidelberg, 2004.
 205. Ralph H. Young. Dipolar lattice model of disorder in random media analytical evaluation of the gaussian disorder model. *Philosophical Magazine Part B*, 72(4):435–457, 1995.
 206. Hiroyuki Yoshida and Kei Yoshizaki. Electron affinities of organic materials used for organic light-emitting diodes: A low-energy inverse photoemission study. *Organic Electronics*, 20:24–30, 2015.
 207. X. Zhou, D. S. Qin, M. Pfeiffer, J. Blochwitz-Nimoth, A. Werner, J. Drechsel, B. Maennig, K. Leo, M. Bold, P. Erk, and H. Hartmann. High-efficiency electrophosphorescent organic light-emitting diodes with double light-emitting layers. *Appl. Phys. Lett.*, 81(21):4070–4072, 2002.